A Modular Atomic Force Microscope for Nanotechnology Research

by

Andrew Careaga Houck

B.S., University of California, Los Angeles (2013)

Submitted to the Department of Mechanical Engineering
in partial fulfillment of the requirements for the degree of

Master of Science in Mechanical Engineering

at the

MASSACHUSETTS INSTITUTE OF TECHNOLOGY

June 2015

Signature redacted

Author .....
Department of Mechanical Engineering
May 18, 2015

Certified by ..... Signature redacted .....
Kamal Youcef-Toumi
Professor
Thesis Supervisor

Signature redacted

Accepted by .....
David E. Hardt
Chairman, Department Committee on Graduate Theses

A Modular Atomic Force Microscope for Nanotechnology Research

by

Andrew Careaga Houck

Submitted to the Department of Mechanical Engineering
on May 18, 2015, in partial fulfillment of the
requirements for the degree of
Master of Science in Mechanical Engineering

Abstract

The atomic force microscope (AFM) has become an essential tool in a wide range of fields, from materials science and semiconductor research to molecular biology. Various research efforts have enhanced the capabilities of this powerful instrument, which has enabled new insights into nanoscale phenomena. Despite decades of research, state-of-the-art AFMs are not widely utilized. In order to accelerate the proliferation and development of these instruments, a modular atomic force microscope is presented. The optical, mechanical, and instrumentation components of the AFM can all be easily exchanged. The instrument can be reconfigured for fundamentally different imaging tasks and can be used as a platform for continued research efforts. The optical beam deflection (OBD) setup can be configured for coaxial or off-axis detection for use with cantilevers of any size. A simple and low-cost design is presented, and an AFM is implemented based on the design. The instrument is tested in two different imaging configurations. First, a configuration for high-speed imaging with small cantilevers is used to image copper deposition on gold in contact mode in liquid. Second, a configuration for large cantilevers is used to visualize the mechanical properties of a polymer blend in tapping mode in air.

The flexibility of the modular instrument is leveraged to develop a new capability for high-speed AFM. Multi-actuated and dual-actuated sample scanners have enhanced the high-speed performance of AFMs by combining multiple nanopositioners with different range and bandwidth characteristics. While this and other improvements have made AFM scanners effective for high-speed imaging, out-of-plane sensing has not been developed adequately. Out-of-plane sensing enhances the capability for quantitative in situ analysis by measuring changes in sample thickness during dynamic processes. This is especially useful in materials science and electrochemical applications, in which understanding of changes in bulk sample thickness is essential. A sensing methodology for high-speed dual-actuated out-of-plane positioning is presented. A silicon-type strain gauge is used to measure the displacement of the low-frequency nanopositioner. A piezoelectric sensor is used to measure high-frequency displacement. The sensor is incorporated into a novel diaphragm flexure nanoposi-

tioner with annular piezoelectric actuator. Fusion of the two sensors for high-speed imaging tasks is discussed. Performance of the two sensors is evaluated, and further developments to integrate the sensing methodology into the modular atomic force microscope are discussed.

Finally, the modular AFM is used in two dynamic nanoscale imaging tasks. High-speed atomic force microscopy has enabled many novel discoveries across a range of applications, especially in biological fields. However, applications in materials science and electrochemistry have not been as thoroughly explored. First, electrochemical deposition of copper on gold during cyclic voltammetry (CV) trials is studied. Electrochemical data from a potentiostat during the CV trials collected in parallel with the AFM images to enrich the analysis. The effect of different initial surface conditions on deposition and stripping is observed. Second, calcite dissolution in low-pH environments is imaged. Dissolution processes in sulfuric and hydrochloric acid solutions are compared. It is apparent that the rhombohedral crystalline structure of the calcite clearly influences the dissolution kinetics in both cases. Erosion of thick calcite terraces is observed in both solutions. However, differences in the dissolution kinetics suggest that the anions play an important role in the process. Multi-actuated sample scanners are particularly well-suited for these two applications, as they involve rapid changes in features at the nanometer scale (e.g. calcite monolayer etch pits and copper nucleation sites) as well as the micron scale (e.g. calcite terraces and copper grains).

Thesis Supervisor: Kamal Youcef-Toumi
Title: Professor

Acknowledgments

I would like to thank my advisor, Professor Kamal Youcef-Toumi. Kamal has been a great advisor and role model over the past two years, and I am lucky to have had the chance to work with him. I would also like to thank Iman Soltani Bozchalooi. This work would not have been possible without his constant support and guidance. Thank you to Jwaher Al Ghamdi for all her help and guidance, and to Axel Paugam-Goering for his work with the AFM team. I would also like to thank Leslie Regan and Catherine Hogan for their administrative support, and Pierce Hayward for his guidance in the graduate machine shop. Many thanks to all the members of the Mechatronics Research Laboratory for making the lab a supportive and creative environment. Finally, thank you to my friends and family for their love and support.

Contents

List of Figures

Chapter 1

Introduction

1.1 Modular Design of an AFM

The atomic force microscope has become an essential instrument in fields ranging from molecular biology to materials science. The atomic resolution of the instrument, combined with its flexibility to image samples in air, aqueous solution, or vacuum, makes it a powerful instrument. Many research efforts have led to enhancements of conventional AFMs, which have in turn led to a wealth of new discoveries. Although these improvements have been pursued by various research groups for several decades, state-of-the-art AFMs are not widely utilized. The high cost and complex nature of these instruments are among the reasons inhibiting more rapid proliferation and development of this technology. In order to make this powerful technology available to a wider group of laboratories and accelerate AFM research, a modular atomic force microscope is developed. All of the optical, mechanical, and instrumentation components of the instrument can be easily replaced. Because of its modular design, the AFM can be used as a platform for continued research. It can be reconfigured for fundamentally different imaging tasks. The optical beam deflection (OBD) setup can be configured for coaxial or off-axis detection for use with cantilevers of any size. All OBD components, including the laser diode, photodiode circuitry, mirrors, and lenses can be easily exchanged. The structure of the instrument can be easily adjusted to accommodate sample scanner of various sizes and types. A simple and low-cost

modular instrument design is presented, and an AFM is implemented based on the presented design. The instrument is tested in two different imaging tasks. First, realtime imaging of metal deposition is performed using a high-speed multi-actuated scanner, coaxial laser detection and a small AFM probe in contact mode in liquid. After reconfiguring the instrument, imaging of mechanical properties of a polymer blend is carried out using a conventional piezo tube, off-axis laser detection, and a large probe in tapping mode in air.

1.2 Out-of-Plane Sensing for High-Speed AFM

Multi-actuated sample scanner designs have enabled simultaneous high-speed and large-range performance by combining nanopositioners with different speed and range characteristics. This capability has helped to extend the application of atomic force microscopy in the study of dynamic nanoscale processes. While much progress has been made in sample scanner design, the capability for out-of-plane sensing during high-speed imaging remains undeveloped. Out-of-plane sensing has been integrated into metrological AFM systems, but these instruments lack the high-speed imaging capability needed to observe dynamic processes. Development of this type of sensing into high-speed systems would enhance the capability for in-situ analysis of dynamic processes by giving quantitative measurement of changes in sample thickness. Furthermore, integrated sensing would simplify system identification for controller design and tuning. Here, a sensing methodology for dual-actuated samples scanners is presented. A silicon-type strain gauge is used to measure the displacement of the low-frequency nanopositioner. A piezoelectric sensor is used to measure high-frequency displacement. The sensor is incorporated into a novel diaphragm flexure nanopositioner with annular piezoelectric actuator. The stability of the strain gauge at low frequencies is well suited for measuring the large-range actuator, while the high sensitivity and wide bandwidth of the piezoelectric sensor make it ideal for monitoring the fast nanopositioner. Fusion of the two sensors for high-speed imaging tasks is discussed. Performance of the two sensors is evaluated, and further developments

to integrate the sensing methodology into the modular atomic force microscope are discussed.

1.3 Study of Dynamic Nanoscale Processes

High-speed AFM imaging systems have been applied to the study of a wide range of dynamic nanoscale processes. These investigations have yielded many new discoveries, especially in biological fields. However, applications in processes related to material science and electrochemistry have not yet been explored thoroughly. In this part of the work, the presented atomic force microscope is used to study two dynamic nanoscale processes. In the first set of experiments, electrochemical deposition of copper on polycrystalline gold is studied. Electrochemical data from a potentiostat during cyclic voltammetry (CV) trials collected in parallel with the AFM images to enrich the analysis. The effect of different initial surface conditions on deposition and stripping is observed. Calcite dissolution in low-pH environments is imaged in the second set of experiments. Dissolution behaviors in hydrochloric and sulfuric acid environments are compared. It is apparent that the rhombohedral crystalline structure of the calcite clearly influences the dissolution kinetics in both cases. Erosion of thick calcite terraces is observed in both solutions. However, differences in the dissolution kinetics suggest that the anions play an important role in the process. Multi-actuated sample scanners are particularly well-suited for these two applications, as they involve rapid changes in features at the nanometer scale (e.g. calcite monolayer etch pits and copper nucleation sites) as well as the micron scale (e.g. calcite terraces and copper grains).

1.4 Overview of the Thesis

The design of a modular atomic force microscope for nanotechnology research is presented in Chapter 2. A methodology for out-of-plane sensing for high-speed atomic force microscopy is presented in Chapter 3. Studies of dynamic nanoscale processes using the modular AFM are presented in Chapter 4. Conclusions and suggestions

for future work are discussed in Chapter 5. Additional information regarding detection circuitry, laser instrumentation, system electronics, and early sensing concepts is summarized in Appendices A, B, C, and D, respectively.

Chapter 2

Modular Design of an Atomic Force Microscope

2.1 Introduction

Research efforts to improve the performance of conventional atomic force microscopes have enabled unprecedented insights into the nanoscale world. However, given the decades of research in this direction, the technology seems to be far from being widely deployed by research labs around the world. There are several reasons inhibiting the fast progression and application of this technology, one being the multifacetted and complex nature of these powerful microscopes. To make the technology accessible to more research labs and help accelerate progress in this direction, we present a modular atomic force microscope.

2.2 Background and Motivation

Since the invention of the atomic force microscope (AFM) [7, 6], extensive research efforts have focused on the development of technologies that improve the performance and extend the applications of this powerful instrument. These efforts span almost all aspects of AFMs, including optics [28, 27, 69, 68], scanners [12, 4, 5, 76, 71, 59], probes [34, 14, 70, 72, 43], instrumentation [28, 27, 24, 22] and control [1, 61, 58, 57,

40, 60, 25, 42, 64, 36, 47, 17, 26, 21].

These and numerous similar research works have enabled applications such as wideband nanomechanical characterization of cells and tissue [52], high-speed nanofabrication [15], and real-time study of material and biological processes[56, 66, 53, 65, 13, 4, 39]. The majority of these developments have been implemented on commercially available AFM setups [50, 63, 45? , 71, 21, 74]. Relatively few research groups have implemented top-down re-designs of the full AFM system [69, 68, 5, 59].

The wide variety of AFM applications makes it difficult to meet all their distinct requirements in a single setup. Small cantilevers with fast dynamics and minimal spring constants are best suited for high-speed imaging. Focusing lenses with higher numerical aperture (NA) and shorter working distances are required to use these probes. As these lenses compromise detection sensitivity [27], AFM setups designed to operate on small cantilevers are often not used with other types of probes. This significantly limits the range of applications of the instrument as there are hundreds of commercially available large probes with different spring constants, tip geometries, and reflective coatings, each suitable for specific types of experiments. Similarly, the most suitable AFM scanners vary depending on the range, precision and speed requirements of a given measurement task. For example, scanners designed for high-speed operation may not be suitable for larger samples or applications that require high positioning precision or large positioning range. Another important component of an AFM is the cantilever chamber/holder. Many AFM applications need to be conducted in vacuum or in controlled gaseous or liquid environments. The possibility to exchange/renew gas or liquid, control temperature or humidity or accommodate different types of electrodes to control electrochemical reactions may be needed. Due to the wide variety of probe chamber/holder requirements, this part of the AFM is often tailored to the specific instrument design or application. Probe chambers for different applications are typically not accommodated in a given AFM design.

In this work a modular, low-cost, and simple AFM design that can easily accommodate various modifications is presented. The modular setup provides a simple platform for fundamental research on nanopositioning, instrumentation and optical

aspects of AFM and enables application of the AFM in diverse measurement tasks. The OBD system of the proposed design can be rearranged to either the coaxial [68] or off-axis [28] detection configurations. All optical components, including the photodiode circuitry and focusing objective, are mounted independently of one another and can be easily removed or replaced. The space allocated for sample scanner can be adjusted for scanners of any size or type. The design also features an independent platform for the cantilever holder/chamber. An AFM is implemented based on the proposed design. The utility of the design is demonstrated by using two different instrument configurations to perform different imaging tasks. First, an instrument configuration which utilizes coaxial detection, a high-speed scanner, and high NA lens is used to study the electrochemical process of copper deposition on gold in real time with a small cantilever in contact mode. Second, a configuration utilizing off-axis detection, a conventional piezo tube scanner, and low-NA lens is used to visualize the contrast in mechanical properties of a blend of polystyrene and polyolefin elastomers with a large cantilever in tapping mode.

2.3 Modular AFM Design

2.3.1 Conceptual Design

The three essential subsystems of the AFM are the optical head, engagement mechanism, and cantilever holder. The essence of the proposed design is the decoupled nature of these instrument subsystems. Each subsystem can be modified or replaced without affecting the rest of the AFM setup. The flexibility of the design is furthered by making each individual subsystem similarly modular: all of the components are easily accessible and can be modified as needed for research and development purposes.

The first major subsystem of the AFM is the optical head, shown in Fig. 2-1a. This optical setup can be configured for either coaxial (CA) or off-axis (OA) detection methods, enabling use with cantilevers of any size. The design also allows

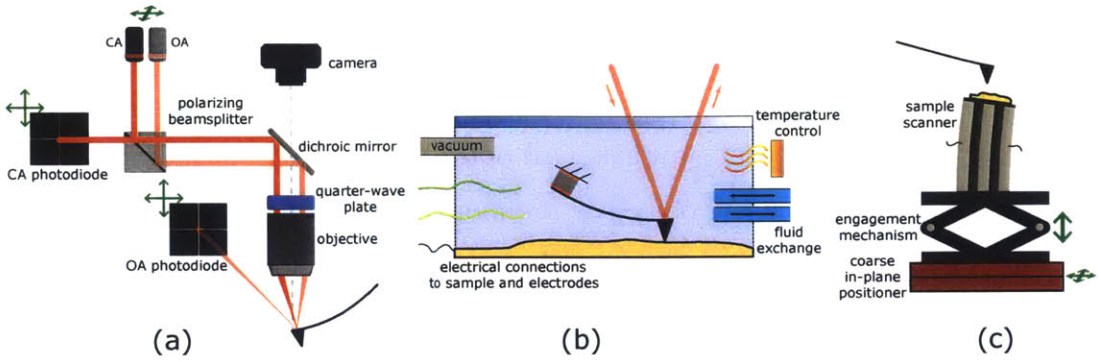

Figure 2-1: Conceptual design of the primary AFM subsystems. a) Optical head, compatible with both coaxial and off-axis OBD methods. b) Probe mounting/holder with a range of features required for different AFM tasks. c) Sample scanner and engagement mechanism.

optical view of the probe during experiments which facilitates laser spot alignment and imaging site selection. The optical head must allow for several adjustment steps during instrument setup. First, the detection circuitry for both CA and OA detection must be adjustable in the plane orthogonal to the incident laser beam to maximize laser signal and zero the deflection signal before imaging.

The required precision of the circuit positioners is determined by the allowable deflection voltage offset before imaging. The adjustment precision of the in-plane position of the laser not as critical, as it is only needed to adjust the incident angle of the laser beam on the probe for switching between detection configurations. Small errors in laser angle can be compensated with the circuit positioners.

Second, the position of the laser source must be adjustable to allow switching between CA and OA detection configurations. Finally, the optical head must be adjustable relative to the probe in XYZ to allow alignment and focusing of the laser spot on the probe tip.

Focus adjustment is critical for instrument performance. The required resolution of focusing adjustment can be calculated by considering the beam cross-section near the focal point assuming a Gaussian beam profile. The diameter of the focused beam at distance z from the beam waist is given by the equation

$$w(z) = w_0\sqrt{1 + \left(\frac{z}{z_R}\right)^2} \tag{2.1}$$

where $w(z)$ denotes the beam radius at position z. w_0 is the beam waist and z_R is the Rayleigh range. These are given by $w_0 = \lambda/(\pi(NA))$ and $z_R = \lambda/(\pi(NA)^2)$. The distance from the beam waist, z', at which the focused spot will just fit on the probe surface is found by solving the rearranged equation where $w(z') = w_{probe}/2$. The total range over which the focused spot fits on the probe determines the required positioning resolution R_f:

$$R_f = 2z' = 2z_R\sqrt{\left(\frac{w_{probe}}{2w_0}\right)^2 - 1} \tag{2.2}$$

The second major subsystem of the AFM is the probe chamber/holder. Robust mounting of the chip and an unobstructed laser path to the probe are essential. Other requirements depend on factors such as imaging mode and sample type. Fig. 2-1b shows a conceptual cantilever holder design with several features commonly required in AFM tasks, such as temperature control and fluid exchange. The versatility of the instrument is increased significantly by designing the probe chamber/holder independently of the other subsystems, since it allows a single instrument to accommodate a wide variety of imaging environments and probe mounting/actuation types.

The sample scanner and engagement mechanism, shown in Figure 2-1c, form the final subsystem of the AFM design. This subsystem drives the sample into contact with the probe, and allows several additional adjustment steps. The in-plane position of the scanner is adjustable to allow for sample site selection during imaging. The scanner can also be rotated for further flexibility and experimental convenience.

2.3.2 Implementation

The modular design is implemented to build an AFM suitable for imaging with both small and large cantilevers. Standard components are used wherever possible to add flexibility and minimize cost.

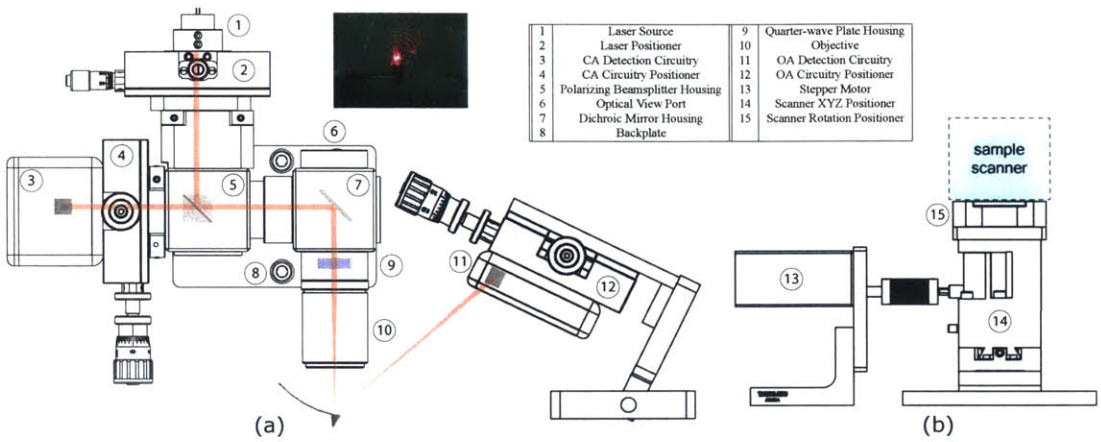

Figure 2-2: AFM subsystems. a) Optical head. This setup allows both CA and OA OBD configurations, and allows access to all optical components and detection circuitry. b) Engagement mechanism. The assembly is compatible with a wide range of scanner types, and offers scanner adjustment in-plane for imaging site selection, as well as rotational adjustment.

AFM Subsystems

The optical head is shown in Fig. 2-2a. Standard 1-inch optical mounts (Thorlabs) house the polarizing beamsplitter (Edmund 48-999), dichroic mirror (Edmund 69-192) and quarter-wave plate (Edmund 46-552). The optical mounts are mounted to an aluminum backplate. Sorbothane gasketing is used to minimize vibration. Custom-made photodiode (Hamamatsu 5980) detection circuits with 3 MHz and 700 kHz bandwidths are used for the small and large probe configurations, respectively. A 670 nm 5 mW laser diode (VPSL-0670-005-X-5-B) is used. The laser current is RF-modulated to reduce optical feedback and interference noise[28, 27].

A high-precision manual positioner with resolution of 0.5 μm/division (Thorlabs ST1XY-D) is utilized for photodiode position adjustment. A manual positioner with resolution of 10 μm/division (Thorlabs ST1XY-S) is selected for laser position adjustment.

The cantilever holder is mounted in an adapter plate which is compatible with a standard optical breadboard. This allows for use with custom cantilever holders, such as the electrochemical cell described in Section 2.4.1, as well as commercially available cantilever holders.

The engagement assembly is shown in Fig. 2-2b. The positioner allows fully vertical engagement, which simplifies operation and minimizes setup time. The resolution of the mechanism must be fine enough to avoid damaging the probe during engagement. In this design, a 200-count stepper motor (Vexta PK223PB-SG36) with 36:1 reduction actuates an 80 TPI Z-axis positioner (Newport DS40-XYZ), resulting in an engagement resolution of 44 nm/step. This corresponds to approximately a 0.25 deg deflection of a 10 μm probe, sufficiently low to avoid damage. The reduction ratio of the gearbox could be reduced further if more precise engagement is desired, with the resolution ultimately limited by friction in the drivetrain. The engagement stepper motor is easily accessed and replaced. In-plane scanner translation is performed via two thumb screws with resolution of 0.3175 mm/revolution. The sample scanner is mounted to a manual rotational stage (Thorlabs MSRP01), which connects to the XYZ positioner via an adapter plate.

Instrument Assembly

Assembly of the AFM subsystems is depicted in Figure 2-3a. The instrument structure is composed of two aluminum optical breadboard decks, joined with steel columns. The optical head is mounted to a three-axis positioner (Thorlabs MT3) for laser spot positioning and focusing.

Using Eq. 2.2, the required focusing precision for a high-NA lens (NA = 0.3) and small cantilever (w_{probe} = 10 μm) is $\sim$28 μm. A positioner with a positioning resolution of 25 μm/division is selected to meet this requirement. This assembly is then mounted to the upper deck of the instrument. The cantilever holder also mounts to this platform, which is machined to allow access between the probe and sample scanner. The scanner and engagement assembly are mounted on the bottom deck. The two-deck design ensures stability and easy access to all instrument components. Furthermore, the spacing between decks can be easily adjusted to accommodate different sample scanners. Sorbothane hemispheres bonded to the underside of the lower deck provide vibration damping. The instrument sits on a vibration table for further vibration reduction. A camera (Canon Rebel SL1) used to observe the probe is mounted

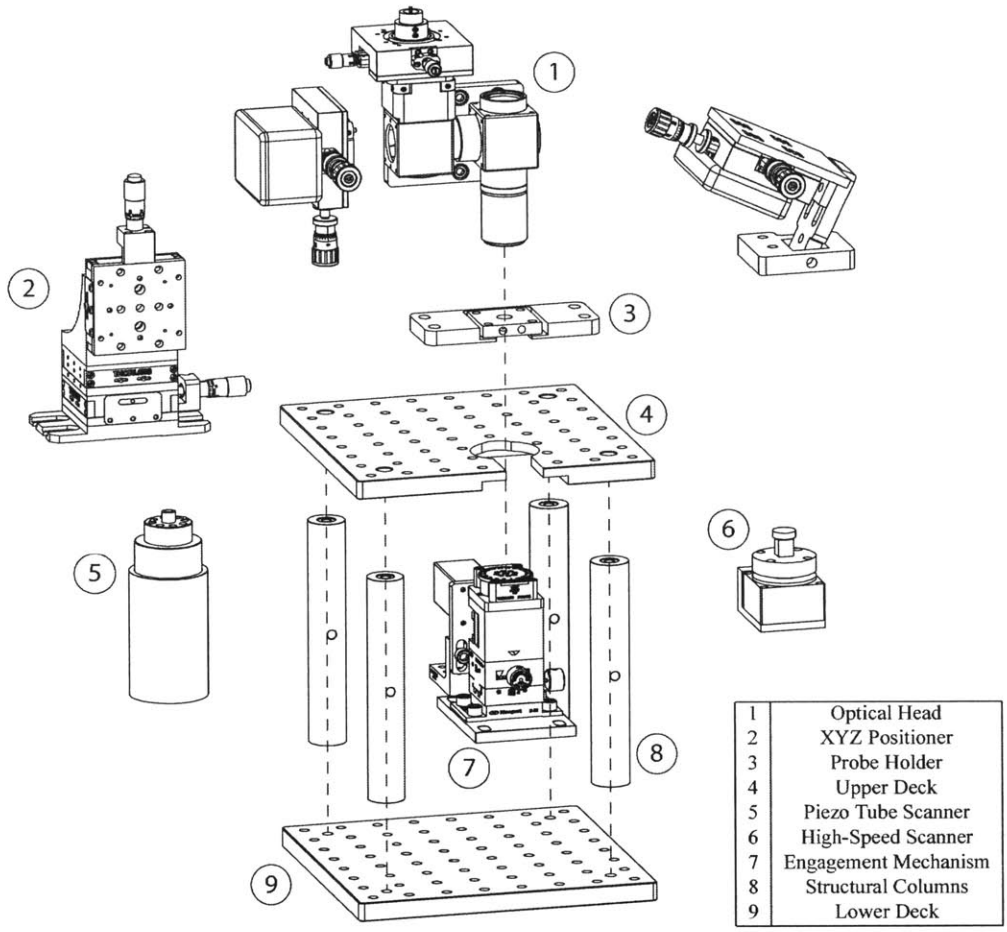

Figure 2-3: Assembly of the AFM subsystems into the final instrument. A two-deck design is used, which facilitates access to the various instrument components. The spacing between decks can be adjusted to accommodate different scanners.

on a separate structure and adjusted with a focusing rack. The camera setup is completely separate from the rest of the instrument and can easily be replaced by a wide variety of optical systems for observation of the probe. The configuration of the instrument can be changed very easily to switch between different applications. Two such configurations are presented in the following section.

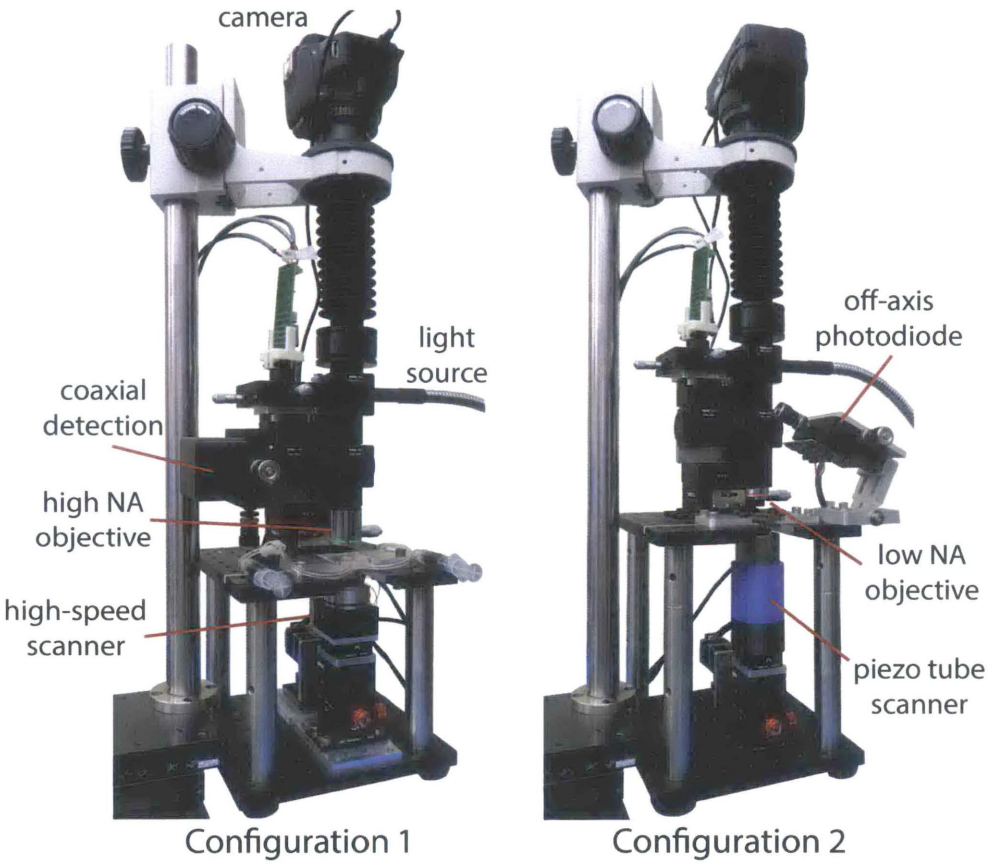

Figure 2-4: Two instrument configurations used for different imaging tasks. Configuration 1 is best suited for fast imaging with small cantilevers, and utilizes a high-speed sample scanner, coaxial detection, and high NA focusing lens. Configuration 2 is suited for use with large cantilevers, and features off-axis detection, a conventional piezo tube scanner, and low NA objective.

2.4 Experimental Evaluation

In this section we utilize the instrument configurations shown in Fig. 2-3 to perform imaging tasks with fundamentally different requirements. First, deposition of copper on a gold substrate is imaged in contact mode in liquid at high-speed. The second imaging experiment is done in tapping mode in air on a polymer blend to compare the mechanical properties of each constituent. Figure 2-3b shows a setup for use with small cantilevers, a high-NA objective (Nikon SLWD L-Plan 20X), and high-speed sample scanner. Figure 2-3c shows a configuration for large cantilevers, low-NA objective (Olympus Plan N 4X), and a piezo tube scanner.

2.4.1 High-speed Imaging of Copper Deposition

The AFM setup presented in Fig. 2-3b is utilized to image the electrochemical process of copper deposition on a gold substrate at high speed. The optical arrangement is configured for CA detection. A small cantilever (10×20 μm) with a spring constant of 0.7 N/m is used to capture nucleation and growth of copper in contact mode at 256 lines/second. A multi-actuated scanner designed to operate at high speed is used.

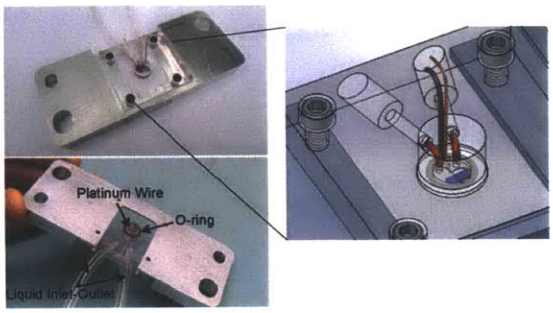

Figure 2-5: Electrochemical fluid cell and cantilever holder. The chamber is composed of optical acrylic and allows mounting of electrodes in the imaging environment, as well as fluid exchange.

The cantilever chamber accommodates a platinum wire as a reference electrode and a copper wire as the counter-electrode (both 0.5 mm diameter, Sigma Aldrich). The working electrode is a piece of gold coated silicon wafer with <111> crystallographic orientation. Figure 2-5 demonstrates the electrochemical cell used in the experiment. The cell is composed of optical acrylic. The thickness of the top layer (1.5 mm) is minimized to avoid excessive displacement of the laser focal plane. The cantilever seat is surrounded by a flexible o-ring that seals the cantilever chamber when in contact with the sample stage to form an electrochemical cell. An inlet and an outlet are incorporated into the chamber to enable continuous refreshing of the copper salt solution in the electrochemical cell. This is performed manually with syringes. All the electrodes are connected to a Parastat 4000 (Stanford Research) potentiostat to control the electrochemical process. Figure 2-6 shows a time-lapse image of the copper deposition over a 5 second interval. Deposited grains nucleate along parallel lines, suggesting some regular structures on the sample which are favorable for deposition.

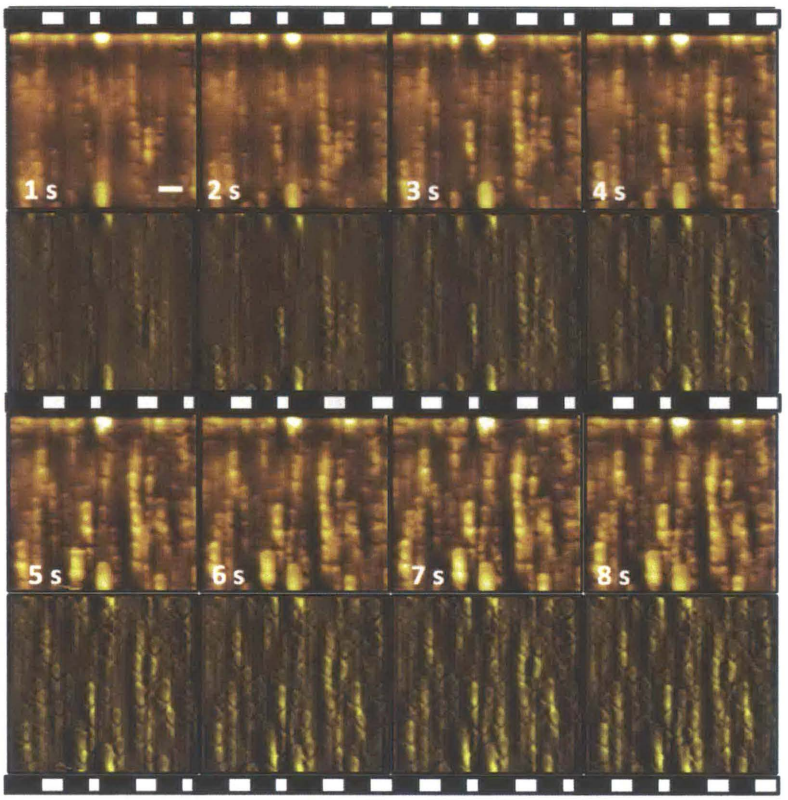

Figure 2-6: Imaging of copper deposition on gold substrate captured at 256 lines/second. A small cantilever (10 × 20 μm) with a spring constant of 0.7 N/m is used in contact mode. Scale bar is 300 nm.

Additional results and discussion from copper deposition on gold trials is presented in Chapter 4.

2.4.2 Imaging Mechanical Properties of Polystyrene-Polyolefin Blend

Next, a sample of polystyrene-polyolefin blend is imaged in tapping mode in air using the configuration shown in Fig. 2-3c. Polystyrene is significantly stiffer (elastic modulus ~2 GPa) than to polyolefin (elastic modulus ~0.1 GPa). This contrast in mechanical properties can be captured in tapping mode phase images. However, the selected probe needs to be relatively stiff in order to capture the contrast. As such, we use a large probe (35 × 225 μm) with a spring constant of 5.6 N/m. The AFM is rearranged to OA optical beam deflection detection as shown in Fig. 2-1 to maximize

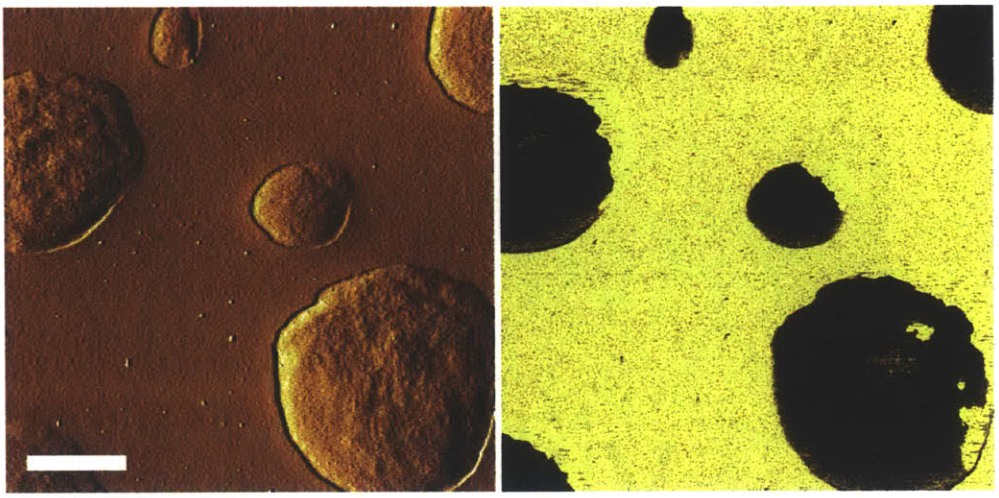

Figure 2-7: Imaging of two-phase polymer in air. a) Height image. b) Phase image showing sharp contrast between the two polymer types, indicating differences in stiffness. Scale bar is 600 nm.

deflection sensitivity. A piezo tube sample scanner is used (Fig. 2-3). This is one of the most common scanner types in atomic force microscopes, and is representative of what may be available to laboratories which utilize conventional AFMs. A commercially available (Bruker MFMA) probe holder suitable for imaging in air is used. The instrument can be easily adjusted to accommodate a range of commercially available sample scanners and probe holders. Since all photodiode circuit signals are accessible, commercial controllers can be integrated easily as well. In this case, the deflection signal is fed to a Nano-Scope IV controller that is used to drive the piezo tube and acquire the AFM images. Figure 2-7 shows the height and phase images. While the height image visualizes the boundaries between polymer constituents, it indicates nothing about any differences in their mechanical properties. The phase image can be used to visualize the difference in elasticity. The phase shift between the cantilever driving signal and the actual cantilever oscillation is affected by the stiffness of the sample. Here, the soft polyolefin regions appear dark, while the stiff polystyrene areas appear bright. The phase image shown in Fig. 2-7 captures the difference with sharp contrast.

2.5 Summary

A modular atomic force microscope is presented in order to accelerate development in AFM-related fields. The design is implemented to create an AFM suitable for imaging with both small and large cantilevers. High-speed contact mode imaging of copper deposition on gold substrate and tapping mode imaging of a polystyrene-polyolefin blend validate instrument performance in two different configurations. The design can easily be extended to suit the needs of myriad applications.

Chapter 3

Out-of-Plane Sensing for High-Speed Atomic Force Microscopy

3.1 Introduction

Multi-actuated scanner designs have proven effective in simultaneously achieving high-speed and large-range AFM imaging performance by combining nanopositioners with different range and bandwidth characteristics. These scanners have enabled new insights into dynamic nanoscale processes. While many improvements have been made in sample scanners, out-of-plane sensing for high-speed use has not been adequately developed. While this capability exists in some metrological AFMs, these instruments typically have low tracking bandwidths not suitable for high-speed imaging of dynamic processes. Out-of-plane sensing enhances the capability for quantitative in-situ analysis by correcting for hysteresis and drift effects in topography images. For example, bulk dissolution rates can be measured in-situ, and correlated with nanoscale surface features measured with deflection images to yield new insights into dissolution kinetics. Furthermore, measurement of out-of-plane position over a wide actuation bandwidth and the full scan range simplifies the process of system identification for controller design and tuning. A sensing methodology for dual actuated out-of-plane positioning for high-speed atomic force microscopy is presented in this work.

3.2 Background and Motivation

High-speed imaging capability extends the application of atomic force microscopy (AFM) to the domain of dynamic nanoscale processes. The research potentials of this new generation of instruments have motivated various research efforts in high-speed AFM [2, 3]. These efforts have yielded significant improvements in AFMs, and have enabled novel scientific observations [39, 67].

Sample scanner performance is critical to high-speed atomic force microscopy, and its improvement is among the most challenging aspects of high-speed AFM research. Research in scanner design and control has led to improvements in bandwidth and reduction of tip-sample interaction forces [10, 12, 57]. Dual and multi-actuation methodologies extend the capabilities of the sample scanner by combining nanopositioners with different range and bandwidth characteristics, and have enabled high-speed, large-range imaging [63, 10, 41, 17, 60, 11].

Various types of high resolution sensors, such as capacitive probes and piezoelectric strain sensors [19, 49], have enabled improvements in scanner performance. While charge mode piezoamplifiers can obviate sensing in some cases, they do not eliminate hysteresis completely and can require complex implementation [51]. Piezoelectric strain sensors are commonly used, as their high sensitivity and low noise at high frequencies makes them well suited for dynamic measurement [29, 20, 23, 77]. Position and force feedback have been used to actively damp scanner resonances and eliminate actuator nonlinearity [23, 46, 20]. In addition, sensor fusion has been used to combine multiple sensor types, utilizing the best characteristics of each [46].

Although implementation of these sensors has brought about significant improvements in scanner capability, out-of-plane sensing has yet to be developed adequately for high-speed use. Accurate out-of-plane sensing enables closed-loop positioning control, simplifies control design and tuning, and enables novel scientific measurements. This capability exists in some metrological AFMs, but these instruments typically have low tracking bandwidths not suitable for high-speed imaging of dynamic processes. For example, bulk dissolution rates can be measured in-situ, and correlated

with nanoscale surface features measured with deflection images to yield new insights into dissolution kinetics.

Our instrument can be used on any process, and will bridge the gap between analysis of nanoscale and bulk phenomena. Previous studies have dealt with a lack of sensing by using the substrate as a reference, which only allows imaging of samples 1-2 microns thick, or by imaging processes where surface roughness can be correlated to film thickness. The out-of-plane actuators are often the fastest and shortest-range of all in a sample scanner, which makes accurate sensing difficult. Additionally, a sensory technique suitable for multiple out-of-plane actuators is required as high-performance setups with multiple actuators become more common.

3.3 Sensors for Dual Actuation

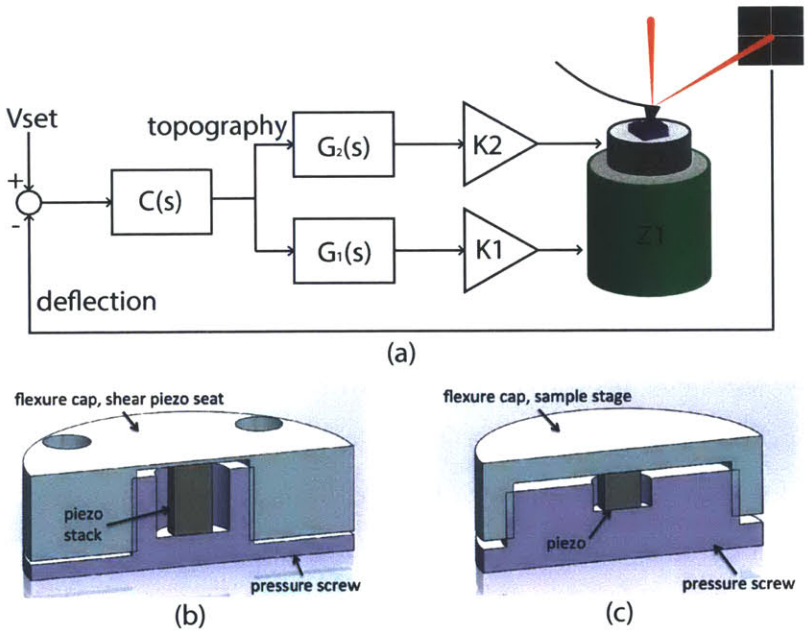

Figure 3-1: a) Dual out-of-plane actuation block diagram. Filters $G_1(s)$ and $G_2(s)$ divide the control effort between the two actuators, sending low-frequency content to $Z1$ and high-frequency content to $Z2$. b) 1-DOF diaphragm flexure type nanopositioners used in high-speed AFM.

To develop out-of-plane sensing for high-speed atomic force microscopy, we begin

by considering the dual actuation methodology, shown in Fig. 3-1a. In its simplest form, the control effort is divided between two actuators using filters $G_1(s)$ and $G_2(s)$. These are typically complementary filters, and effectively pass low-frequency content to Z_1 and high-frequency content to Z_2. The filter outputs are amplified and passed to the actuators, assuming that all dynamics occur at high frequencies outside of the actuation band. In the multi-actuated case, $G_1(s)$ and $G_2(s)$ also compensate for unwanted nanopositioner dynamics. A sensor for each actuator, as well as a method for fusing the two signals into a single measurement of out-of-plane position, are needed. Figures 3-1b and c show examples of Z_1 and Z_2 nanopositioners used in this type of setup, respectively. The range and bandwidth characteristics are representative of those typically found in high-speed setups. The Z_1 positioner typically has a bandwidth on the order of kHz, and a range of up to 20 μm. Z_2 nanopositioners have been demonstrated with bandwidth up to 150 kHz, with typically range of 1-2 μm [75].

3.4 Low-Frequency Actuation and Sensing

During imaging, the low-frequency actuator compensates for large features with low spatial frequencies such as sample tilt and thickness. Actuators of this type typically have bandwidths on the order of several kilohertz, and maximum ranges of 10-20 microns. A strain gauge sensor is well suited for these frequency and displacement requirements. Since this type of sensor is bonded directly to the actuator itself, it can be integrated into any existing actuator design which utilizes a piezoelectric actuator, including the diaphragm flexure nanopositioner as shown in Fig. 3-2a. In addition, multiple strain gauges can be bonded to a single actuator, enabling the use of several different bridge designs for temperature compensation, nonlinearity correction, etc. For simplicity, a single silicon type strain gauge is utilized here. This type of strain gauge offers a significantly higher gauge factor than conventional metal foil gauges. Here, the strain gauge with resistance R_{sg} forms the feedback resistor of a differential amplifier circuit, shown in Figure 3-2b. When the circuit resistors are matched,

$R_1 = R_2 = R_3 = R$, the amplifier transfer function is as follows:

$$\frac{V_o(s)}{V_i(s)} = \frac{1}{2}\left[1 - \frac{R_{sg}}{R}\frac{1}{R_{sg}C_f s + 1}\right] \tag{3.1}$$

where V_i is a DC input voltage. Assuming the low-pass pole is kept far from the actuation band, the sensor output can be calculated with the DC gain of the transfer function:

$$\frac{V_o}{V_i} = \frac{1}{2}(1 - R_{sg}/R). \tag{3.2}$$

This design can be thought of as an active bridge circuit, and ensures a linear response in the desired actuation frequency range with a single strain gauge. The feedback capacitor, C_f, should be selected to produce roll-off one decade above the maximum actuation frequency to avoid phase lag. An additional amplifier stage can be used to amplify the signal and allow offset nulling.

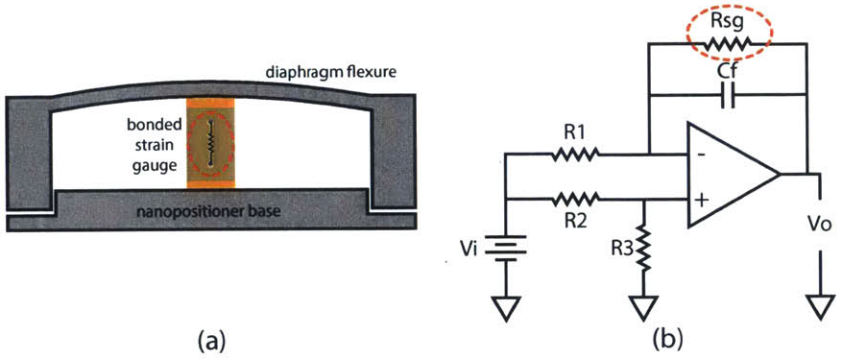

Figure 3-2: Strain gauge circuit for low-frequency displacement sensing. This configuration ensures a linear response using a single silicon-type gauge.

3.5 High-Frequency Actuation and Sensing

The high-frequency actuator compensates for smaller surface features with high spatial frequencies. Piezoelectric actuators are particularly suitable for nanopositioners of this type due to their wide bandwidth and low profile. These nanopositioners have been built with bandwidths up to 150 kHz [38]. Actuation range is typically on the order of 1-2 microns. Diaphragm flexure designs, as shown in Fig. 3-3a are commonly

used. In addition to their high-frequency dynamics, the encapsulated design protects electrical connections from stray liquid when imaging in aqueous environments, and can have very low mass. The mass of the high-frequency actuator and sensor must be kept small to avoid reducing the bandwidth of the other positioners in the sample scanner or causing excessive dynamic forces at high-speed.

Retroactive enhancement of these nanopositioners, as in the low-frequency case, would be ideal. However, incorporating a sensor directly presents some challenges. Since the actuator sits directly below the sample, it is difficult to measure displacement at the sample itself. A thin film sensor bonded to the diaphragm, such as a piezoelectric polymer transducer, could be used but would measure strain across the entire diaphragm instead of the sample location alone. Alternatively, a sensor could be placed around the actuator inside the cap. Again, this would result in an indirect measurement of sample displacement.

To solve this problem, the centrally located piezoelectric actuator is replaced with an actuator of annular cross-section, as shown in Fig. 3-3b. The annular actuator enables sensing of diaphragm displacement at the sample itself, and increases positioning range due to its higher blocking force. An additional benefit is that the displacement profile of the diaphragm is flattened when using the annular actuator as shown in Fig. 3-3. This makes the performance of the nanopositioner during imaging less sensitive to sample placement. The static displacement of two designs are shown in Fig. 3-3c and d. Here, a square actuator with 2x2 mm cross section is compared with an annular actuator with 4.5 mm inner diameter and 8 mm outer diameter.

A piezoelectric transducer is selected to measure the displacement between the center of the diaphragm and the base of the nanopositioner. This type of transducer is chosen for its low profile, high sensitivity, wide bandwidth, and low noise.

3.5.1 High-Speed Nanopositioner

A bonded diaphragm flexure design is utilized. A positioning bandwidth of 100 kHz and positioning range of at least 1 micron are targeted. An analytical model of a thin circular diaphragm as discussed in [38] is used to select the diaphragm thickness. The

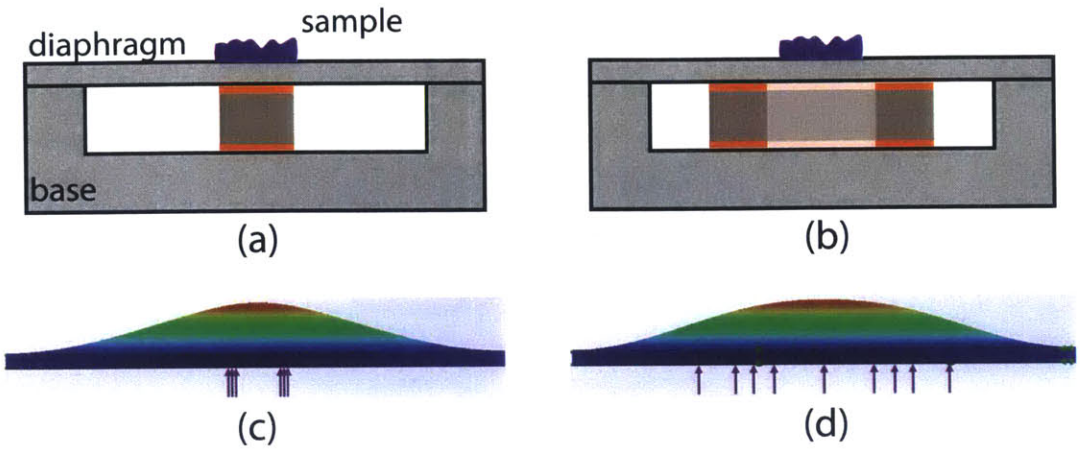

Figure 3-3: a) Conventional diaphragm flexure positioning with central piezoelectric actuator. b) Positioner utilizing annular actuator. c) and d) normalized diaphragm displacement profiles for the conventional and annular actuator designs, respectively.

model assumes a fixed boundary and guided circular constraint at the center. Finite element analysis is then used to validate the design and ensure that the dynamic modes lie outside the desired actuation band.

The equivalent spring constant, k_{eq}, of the diaphragm should be at least one order of magnitude less than the stiffness of the actuator in order to avoid reducing the positioning range. In practice, diaphragms with large spring constants due to small diameter or large thickness tend to introduce erratic dynamics in the diaphragm flexure positioner. A spring constant of 5 N/μm is selected. The analytical model yields a diaphragm thickness of approximately 0.5 mm when using aluminum 6061 (E = 69.9 GPa).

A circular piezoelectric stack actuator with an inner hole (PI PD080.31) is selected. The actuator has an outer diameter of 8 mm, inner hole diameter of 4.5 mm, and thickness of 2.5 mm. The free stroke and unloaded axial resonant frequency of the stack are 2.0 μm and 500 kHz, respectively. A diaphragm diameter of 16 mm is used to overall nanopositioner size while leaving sufficient clearance between the actuator and diaphragm boundary.

FEA software is used to determine the dominant resonant modes of the diaphragm design, shown in Fig. 3-4. The lowest frequency modes begin around 148 kHz. In

addition to considering these modes near the edges of the diaphragm, it is critical to ensure that any dynamic modes at the sample location do not lie within the actuation band.

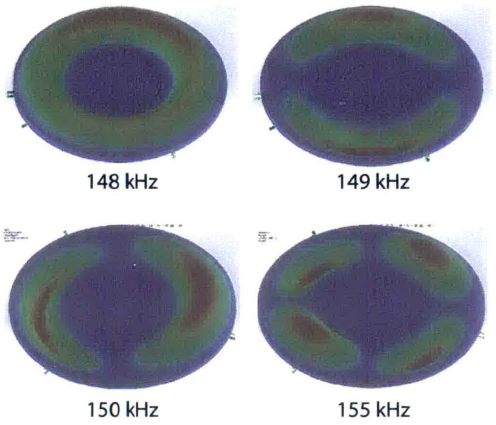

Figure 3-4: Finite-element of the nanopositioner design. The dominant modes begin at $\sim$ 148 kHz.

3.5.2 Piezoelectric Sensor

The sensor and bonding layers are designed to achieve high sensitivity and dynamic performance. For this analysis, a 2x2x2 mm piezoelectric stack (PI PL022.31) with 30 nF capacitance is selected. The overall bonding layer thickness is selected to be 0.5 mm so that the sensor can be bonded between the diaphragm and actuator seat without any changes to the cap design (actuator thickness = 2.5 mm).

The sensitivity is proportional to the equivalent spring constant of the sensor and its bonding layers, k_{eq}. However, k_{eq} is limited in practice, as an overly stiff sensor can compromise the deflection profile of the diaphragm. Static FEA simulation is used to determine the maximum allowable equivalent sensor spring constant, k_{max}, beyond which the sensor will cause a dip in the displacement profile at the sample location. In this case, simulation yields that $k_{max} \simeq 0.2k_{eq}$. The bonding layers on either side of the transducer are designed such that $k_{eq} = k_{max}$ in order to maximize sensitivity without affecting positioning range.

To meet these requirements while ensuring that any sensor dynamics will occur at

high frequencies outside the actuation band, we turn to a lumped parameter model of the sensor and bonding layers, as shown in Fig. 3-5a. The transducer and upper and lower bonding layers can be modeled as two equivalent half masses. Each layer has its own spring and damping constants. The assembly is attached to ground at one end, representing the base of the positioner, and a moving connection point at the other, representing the diaphragm at the sample location.

This model can be simplified to ease analysis. First, the piezoelectric actuator is assumed to be very lightly damped, so $k_2 \to 0$. Additionally, the spring constant of the piezoelectric ceramic is very large compared to the bonding layers, so $k_2 \to \infty$. Now the spring and damping characteristics of the bonding layers are our only design parameters, as shown in Fig. 3-5b.

To achieve a sufficiently low spring constant while maintaining a high sensor resonance frequency, the natural solution is to make one bonding layer very stiff and the other very soft. In the extreme case where $k_3 \to \infty$, the model reduces to a simple force sensor with linear response to displacement as shown in Fig. 3-5c. Any damping of the top layer, denoted b_1, will result in roll-up in the sensor response. However, if the bonding material is sufficiently lightly damped, this will occur at high frequencies outside the desired bandwidth.

The model in Fig. 3-5b is used to select the characteristics of the two bonding layers. It is assumed that both layers are lightly damped, so that $b_1, b_3 \to 0$. First, the equivalent spring constant of the sensor is calculated:

$$k_{eq} = \left[\frac{1}{k_1} + \frac{1}{k_3}\right]^{-1} = h^2 \left(\frac{t_1}{E_1} + \frac{t_3}{E_3}\right)^{-1} \tag{3.3}$$

where k, h, t, and E are the equivalent spring constant, width, thickness, and Young's modulus of each element, respectively. It is assumed that both bonding layers take on the same cross section as the piezoelectric transducer. The axial resonant frequency of the sensor is given by

$$f_{res} = \frac{1}{2\pi}\sqrt{\frac{k}{m_s}} = \frac{1}{2\pi\sqrt{h\rho}}\left[\frac{t_1}{E_1} + \frac{t_3}{E_3}\right]^{-1/2} \tag{3.4}$$

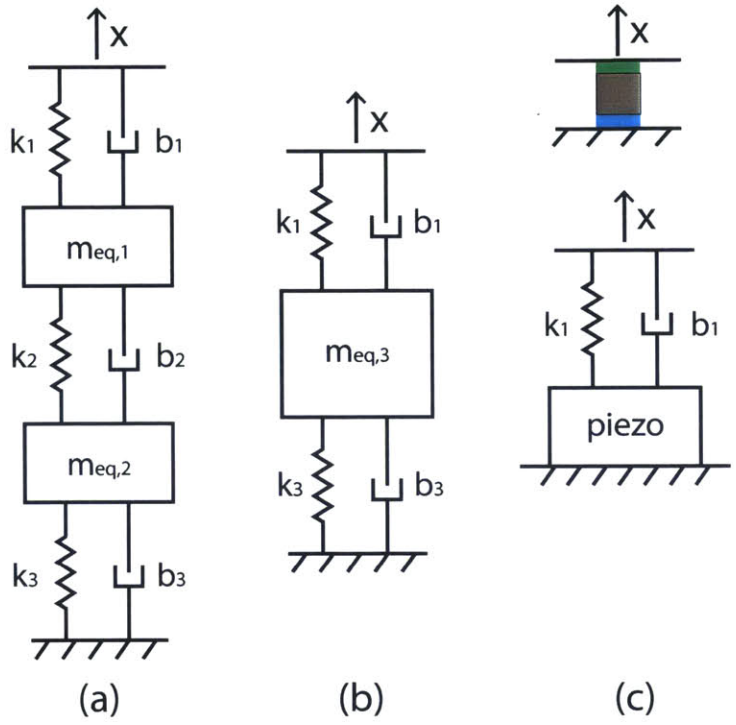

Figure 3-5: Dynamic model of the piezoelectric sensor and bonding layers. a) Lumped parameter model which considers the spring and damping constants of the top bonding layer, piezoelectric transducer, and bottom bonding layer, with subscripts 1, 2, and 3, respectively. b) simplification of the model when assuming a lightly damped, stiff transducer. c) reduction to a simple force sensor with a linear response to displacement as $k_3 \to \infty$.

where m_s is the mass of the piezoelectric transducer. Since Young's modulus data is not typically available for epoxies, Shore D hardness, denoted S_D, is used to select the bonding materials. S_D is related to Young's modulus by the following [55]:

$$\log_{10} E = 0.0235 S_D - 0.6403 \quad 30 < S_D < 85 \tag{3.5}$$

In this case, a cyanoacrylate lower bonding layer (Loctite 401) and epoxy upper layer (DP190) are used, yielding a sensor resonant frequency of ~250 kHz.

3.5.3 Signal Conditioning

The sensor signal is conditioned with a charge mode amplifier, as shown in Fig. 3-6. The piezoelectric transducer is modeled as a charge source with parallel capacitance, C_p, and shunt resistance, R_p. Stray interface cabling capacitance, C_c, is also taken into account. R_p is assumed to be very large. A FET amplifier with low input bias current (ADA4627-1) is used to minimize voltage offset. A guard ring around the inverting input further reduces bias voltages. The voltage output of the amplifier in the passband, V_o, is given simply in terms of the charge input q and feedback capacitance C_f by $V_o = -q/C_f$. The charge input can be expressed in terms of the piezoelectric charge coefficient of the sensor, d, and the force acting on the sensor at a given diaphragm displacement, z, by

$$q = dF = dk_{eq}z. \tag{3.6}$$

The sensitivity of the piezoelectric transducer bonded between the diaphragm and actuator seat is then given by the equation

$$\frac{V}{z} = \frac{dk_{eq}}{C_f}. \tag{3.7}$$

Rearranging, these equations are used to set C_f so that the maximum displacement amplitude of the diaphragm results in the desired maximum amplifier output amplitude V_{max}:

$$C_f = \frac{dk_{eq}z_{total}}{2V_{max}} \tag{3.8}$$

where z_{total} is the total displacement range of the nanopositioner. V_{max} is limited in practice by the rail voltage of the amplifier. The remaining circuit component values are calculated when setting the amplifier pole frequencies. The bandpass break frequencies are selected to be approximately one decade from the actuation band to avoid phase lead/lag at frequencies of interest. The lower and upper break frequencies

of the charge mode amplifier, denoted f_1 and f_2, respectively, are given by

$$f_1 = \frac{1}{2\pi R_f C_f} \qquad f_2 = \frac{1}{2\pi R_i C_s}. \tag{3.9}$$

In this case, the charge mode amplifier amplifies the charge from the transducer and acts as a bandpass filter. The low-frequency is responsible for measurements from DC to 1-2 kHz. The piezoelectric sensor then takes over at high frequencies, eventually rolling off above the mechanical bandwidth of the Z2 positioner.

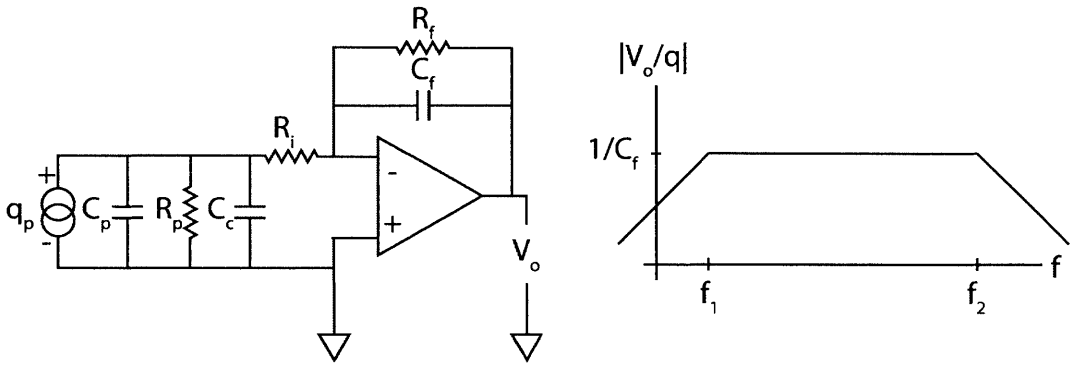

Figure 3-6: Charge mode amplifier. The charge output from the piezoelectric transducer is balanced by a charge on the feedback capacitor. The voltage output in the passband is related simply to the charge input by $V_o = -q/C_f$.

3.6 Sensor Fusion

The two sensors must be fused to provide a unified measurement of position during high-speed imaging. The low-frequency and high-frequency sensors are denoted S_1 and S_2, respectively. The goal of sensor fusion is to use desired characteristics of multiple sensors, which often perform best in different frequency regimes. In this case, the strain gauge measures only low frequency out-of-plane displacement, while the piezoelectric sensor monitors high-frequency content. Normally, these two sensors could be combined by applying methods such as complementary or Kalman filtering [32]. In this case, a complementary fusion technique is adapted to the problem of sensing multi-actuated positioners.

The multi-actuation method itself can be used to simplify the fusion. In multi-actuation, complementary filtering is used to divide the command signal, $\mathbf{U}$, into its low- and high- frequency components, $\mathbf{U_1}$ and $\mathbf{U_2}$, respectively. Since each sensor is only responsible for a single actuator, its response only includes frequency content of interest. As such, gain adjustment is all that is needed to combine the resulting responses, $\mathbf{S_1}$ and $\mathbf{S_2}$ into the combined measurement, $\mathbf{S_f}$:

$$\mathbf{S_f} = K\mathbf{S_1} + \mathbf{S_2} \tag{3.10}$$

where $K = |S_2(j\omega_2)|/|S_1(j\omega_1)|$, and ω_1 and ω_2 are frequencies in the passbands of S_1 and S_2, respectively. It is important to ensure that the phases of the two sensor responses match at the transition frequency when designing the filters to avoid corruption of the fused measurement.

3.7 Results and Discussion

Sensor measurements are validated in this section. A custom-made dynamic signal analyzer is implemented in LabVIEW, and a TechProject amplifier is used to drive the piezo actuators. Comparisons with measurements taken with a laser interferometer with 500 kHz bandwidth (SIOS SP-S 120) are used to assess sensor performance. Random binary sequence (RBS) excitation signals are used in all frequency response function plots.

3.7.1 Experimental Setup

The dynamic response of each sensor is tested independently. Each actuator is excited with a random binary sequence, and the responses are measured with the respective sensor and laser interferometer. The empirical transfer function estimates (ETFE) constructed with the two data sets are compared.

The low-frequency sensing method is tested as part of a custom-made high-speed sample scanner, shown in Fig. 3-7. A piezoelectric stack actuator (PI 885.11) with

bonded silicon strain gauge provides low-frequency out-of-plane positioning. The actuator is preloaded from below with a pressure screw. The scanner will accommodate a high-frequency nanopositioner mounted to the Z_1 flexure structure. Two opposing piezoelectric stack actuators (PI 885.11) provide lateral positioning, and are also preloaded by pressure screws. Lateral range and bandwidth are 5 μm and 6 kHz, respectively. The assembly is designed to be mounted to a commercial nanopositioner (PI P-611.20) for low-frequency lateral and frame up/down positioning with 100 μm range.

A high-speed nanopositioner prototype is tested separately. The base is machined out of aluminum 6061. The diaphragm is cut from an annealed aluminum sheet with 0.5 mm thickness, and is glued to the base under pressure using instant adhesive (Loctite 493). The actuator pocket is machined such that the actuator protrudes $\sim$100 μm to allow sufficient preloading during bonding. The actuator is also bonded to the diaphragm using instant adhesive (Loctite 401).

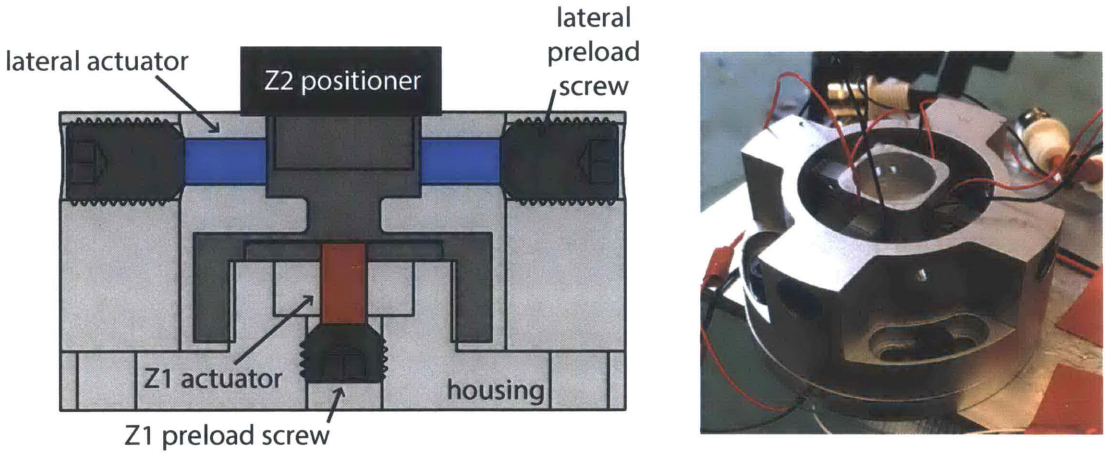

Figure 3-7: Multi-actuated sample scanner. The low-frequency out-of-plane (Z1) actuator displaces a diaphragm flexure, on which the high-frequency (Z2) positioner is mounted. Additional piezo stacks provide lateral motion for high-speed scanning. The assembly is designed to mount on a commercially available XY positioner for low-speed scanning and frame up/down positioning.

3.7.2 Sensor Performance

Figure 3-8 shows the frequency response of the low-frequency nanopositioner and sensor. The blue curve shows the response measured with the integrated silicon strain gauge sensor, while the red curve shows the laser interferometer measurement.

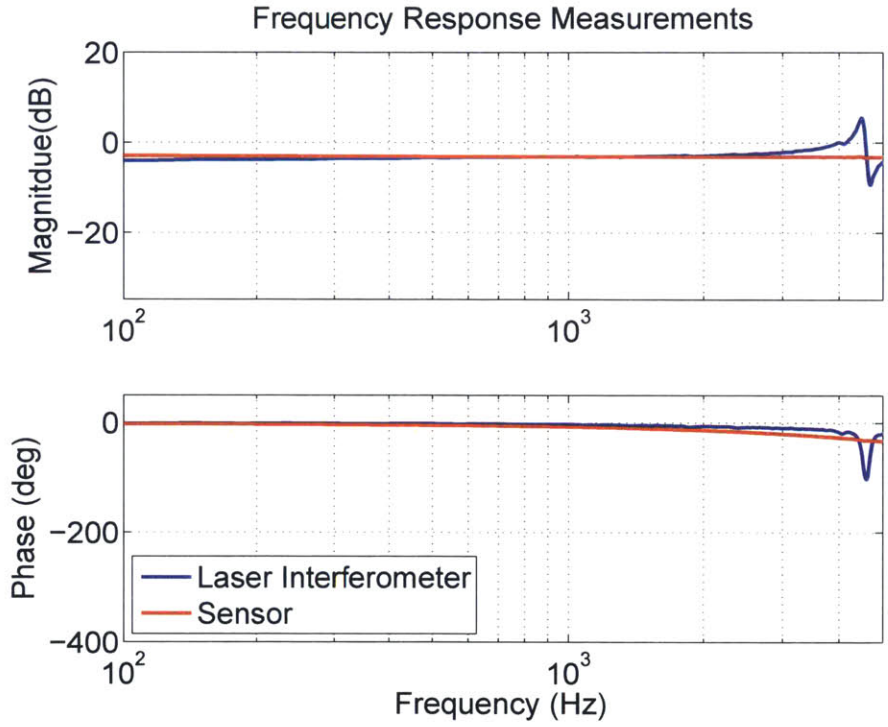

Figure 3-8: Low frequency positioner and sensor response. The sensor tracks the actuator well up to $\sim$ 3 kHz, above the frequencies required for high-speed imaging. The sensitivity is 847.5 mV/μm in the passband. The integrated sensor is blind to the resonance at 4.5 kHz, which occurs elsewhere in the sample scanner.

The sensor response matches the laser reading over the passband with sensitivity of 847.5 mV/μm. The nanopositioner has a total range of 4.5 μm. The sensor tracks well over the desired actuation frequency range (DC to 1-2 kHz). The high-frequency roll-off in the strain gauge circuit does not introduce phase lag in the sensing band. There are some high frequency dynamics in the response measured by the laser interferometer that are not detected by the sensor. These are likely resonances in other parts of the scanner to which the sensor is blind. In any case, they lie outside the actuation band and do not compromise use of the sensor.

The response of the high-frequency nanopositioner and sensor are shown in Fig. 3-9. Overall, the sensor shows good tracking of the positioner displacement. The charge

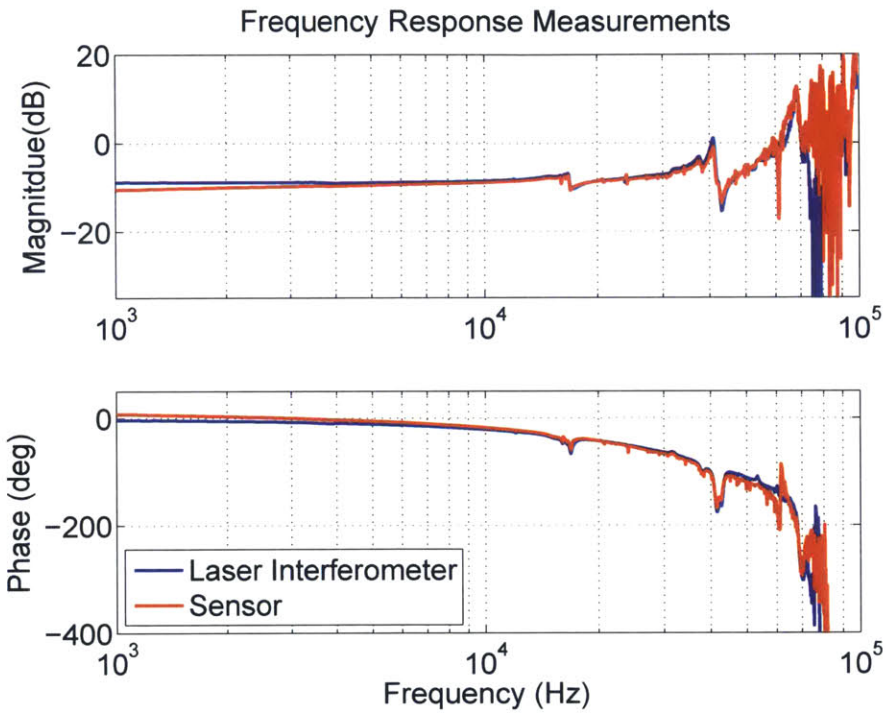

Figure 3-9: High-frequency nanopositioner and sensor response. The sensor tracks the actuator well until $\sim$ 60 kHz. The annular piezoelectric actuator exhibits erratic dynamics above $\sim$70 kHz in all nanopositioner iterations, as well as in isolation.

mode amplifier bandpass limits are set to 150 Hz and 600 kHz. The sensitivity of the sensor is 14.5 mV/nm in the passband. The charge mode amplifier poles do not introduce any phase lead or lag in the actuation band. The nanopositioner has a total range of 1.93 μm, more than enough to track the high-frequency spatial content of samples encountered in practice. However, the actuator shows erratic behavior above $\sim$70 kHz. This behavior is evident in nanopositioner prototypes, as well as in isolation. Replacing the annular actuator with another of wider effective bandwidth is required so that the nanopositioner can be integrated into the multi-actuated sample scanner and used reliably for high-speed imaging and sensing.

3.8 Summary

Recent advances in high-speed atomic force microscopy have extended application of the instrument to imaging dynamic nanoscale processes. Improvements in scanner design and control have enabled new capabilities, and the incorporation of sensing can push these capabilities even further. Out-of-plane sensing enables closed-loop positioning, simplifies controller design and tuning, and allows novel scientific measurements. In this work, an out-of-plane sensing system is developed for dual-actuated out-of-plane positioning.

A silicon type strain gauge monitors the low-frequency positioner, while a piezoelectric transducer measures displacement of the high-speed actuator. An annular piezoelectric actuator and inner piezoelectric transducer are used. The effective bandwidth of the nanopositioner is ~70 kHz with compensation, and the total positioning range is 1.93 μm. Fusion of the two sensors is facilitated by the multi-actuation methodology itself, which reduces the problem to simple gain matching. This type of sensing will extend the capability of high-speed atomic force microscopy in quantitative in-situ analysis.

Chapter 4

Study of Dynamic Nanoscale Processes

4.1 Introduction

High-speed atomic force microscopy has enabled new insights into dynamic nanoscale processes. While the technology has led to many new discoveries, especially in biological fields, applications in material and electrochemical processes have not been as thoroughly explored. In this work, the modular AFM described in earlier chapters is used to study two nanoscale processes in real time.

4.2 Background and Motivation

High-speed atomic force microscopy has enabled many new insights into dynamic processes at the nanoscale. While many research efforts have focused on biological applications, areas of materials science and electrochemistry have not benefitted as much from these powerful instruments. Understanding of these processes at a mechanistic level is critical for countless applications.

Mineral-fluid interaction is central to the behavior of both natural and engineered systems. Understanding of these mineral-fluid interactions is typically limited to only the simplest systems, and there are significant gaps in understanding of the detailed

surface kinetics of these reactions [16]. Electrochemical processes are widely utilized for fabrication of coatings and electronics. Metal dissolution and corrosion is also of critical importance for a vast array of technologies.

Atomic force microscopes are well-suited for studying these phenomena, due to their high resolution and compatibility with samples in aqueous environments. While some indirect measurement techniques exist for studying these reactions, the detailed kinetics can only be studied via direct observation [33].

In this work, two nanoscale processes are studied. First, electrochemical deposition of copper on gold is performed via cyclic voltammetry (CV). Growth behavior of deposited structures is characterized, as well as irreversible surface changes which occur as a result of the CV trials. Second, calcite dissolution is observed in hydrochloric and sulfuric acid solutions at low pH. Dissolution phenomena in these two acid solutions are compared.

4.2.1 Copper Deposition on Gold

Electrochemical metal deposition has countless applications in engineered coatings and electronics. Combining nanoscale observation with electrochemical measurements has enabled new insight into these processes. The growth of hydroxyapatite on titanium [18], deposition of gold on copper [44], and growth of platinum nanocrystals [78] are a few processes that have been studied by combining these techniques.

Copper deposition is a process of particular interest due to its applications in metallization for electronics, and has been observed at the nanoscale using atomic force microscopy [48, 30, 73, 35]. The majority of these studies have used conventional AFMs with very low scan rates. Here, we leverage the high-speed and large-range capabilities of the presented instrument to study copper deposition and stripping on a gold substrate in real time.

4.2.2 Calcite Dissolution

Calcite is extremely common in both natural and man-made systems. The various forms of this carbonate rock play an important role in natural processes at all scales, from local erosion of soil to the shaping of continents [16]. Atomic force microscopy has been utilized to study the dissolution of calcite, as well as other minerals [9]. These studies have focused on aspects such as dissolution and growth mechanisms [33], correlation between microscale processes and macroscopic wetting behavior [37], and calculation of bulk dissolution rates from nanoscale measurements [62].

Calcite dissolution in the low-pH regime is not well understood. This is due to the high rates of reactions in these aggressive acid environments, which have made it difficult to study with conventional AFMs. The high-speed imaging capability of the presented AFM enables new insights into reaction kinetics in low-pH environments. Video-rate imaging of these fluid-mineral systems in low-pH environments has applications in many other important processes, including drug dissolution and dental enamel erosion [54].

4.3 Copper Deposition on Gold

4.3.1 Experimental Setup

A three-electrode electrochemical cell, as shown in Fig. 4-1, is used in these experiments. The cell consists of a working electrode (WE), counter electrode (CE), and reference electrode (RE), which are immersed in the electrolyte. In voltammetry experiments, a potential is applied across the working electrode and counter electrode. The current between these two electrodes is measured as the process takes place. In addition, the potential of the working electrode relative to the electrolyte is measured by using the reference electrode. The sample is a piece of silicon wafer of 500 μm thickness with titanium adhesion layer and 100 nm sputtered gold coating. This type of coating is typically highly crystalline with <111> crystallographic orientation. However, the sample used in this test showed some initial surface roughness, which is

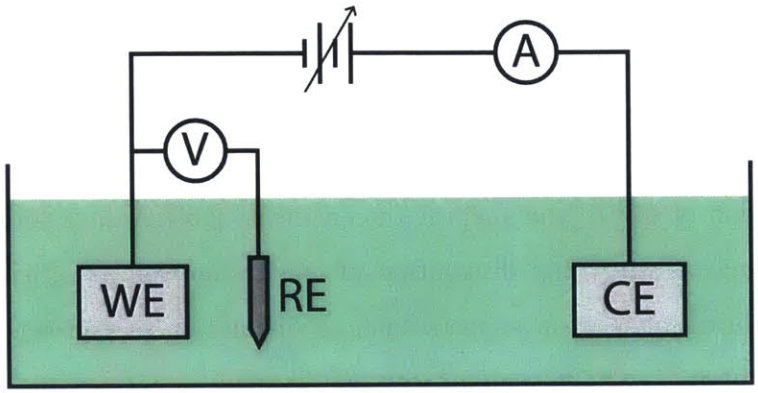

Figure 4-1: Three electrode electrochemical cell. In voltammetry, potential is applied across the working and counter electrodes (WE and CE, respectively). Current across these two is then measured as a function of working electrode potential, which is measured relative to the reference electrode (RE).

indicative of a polycrystalline structure. In this experiment, the gold substrate acts as the working electrode. A platinum counter electrode and copper reference electrode are used. All the electrodes are connected to a Parastat 4000 (Stanford Research) potentiostat to control the electrochemical process. The electrolyte is 5 mM copper sulfate solution. Cyclic voltammetry (CV) is performed during simultaneous high-speed imaging. In this analysis, all potential values are given relative to the Cu/Cu^{2+} electrode potential. A 40 x 40 μm triangular probe with a spring constant of 0.8 N/m (Bruker FastScan C) was used in contact mode in all trials.

4.3.2 First CV on Polycrystalline Substrate

The first CV is performed starting with a clean gold substrate. The starting surface has an RMS surface roughness of 7.1 nm. No underpotential deposition (UPD) phase was observed during these trials. The majority of deposition occurs from potentials of approximately -200 to -400 mV. The development of large copper grains is observed during this period. AFM frames of the nucleation of one of these grains is shown in Fig. 4-2.

The first nucleate occurs at -213 mV, and grows to a final height of approximately 300 nm. The early development of the nucleate is also visualized in three dimensions,

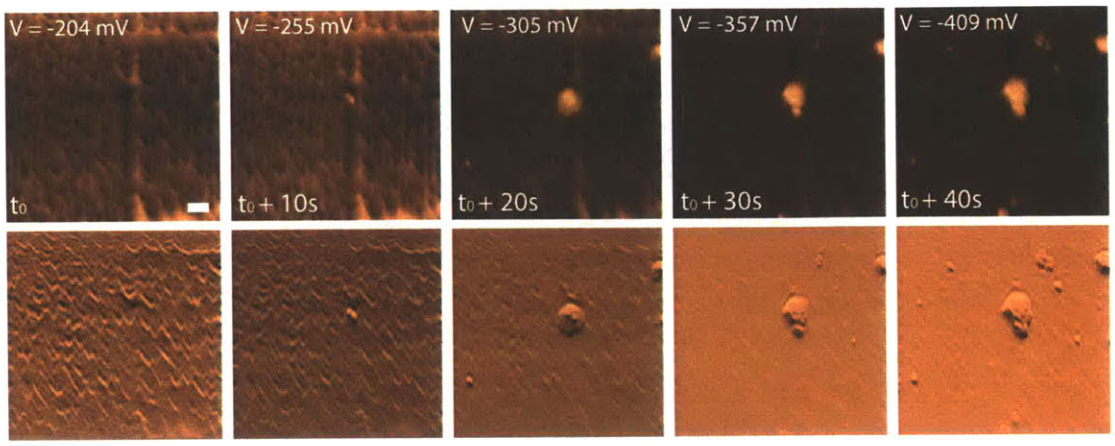

Figure 4-2: Nucleation and growth of a copper grain on gold substrate. Scale bar is 300 nm. The frames were captured at 1 frame per second. Scan speed is 256 lines/second, 1024 samples/line.

as shown in Fig. 4-3.

Nucleation occurs within a small scratch on the substrate which suggests that surface imperfections or indentations may be preferred nucleation sites, as expected. Many large grains form during the deposition process. Figure 4-4 shows the evolution of grain area and volume with time for the grain shown in Figs. 4-2 and 4-3, as well as total number of grains on the surface with time.

An additional phase of the deposition process occurs at potentials of approximately -700 to -800 mV. Several small grains are developed during this part of the process, as highlighted in Fig. 4-5. In addition, increased surface corrugations develop during this period. Figure 4-5 shows three-dimensional images from the beginning and end of this phase, at potentials of -697 and -791 mV, respectively.

The growth of small copper grains and increase of surface corrugations is apparent between the two frames. As a result, the RMS surface roughness increases from 37.8 nm to 45.6 nm. All copper deposits should ideally be stripped away as the potential is swept back to its starting point, however, it is observed that some copper remnants remain on the surface after the CV. The substrate surfaces at the beginning and end of the CV are shown in Fig. 4-6. The RMS surface roughness has increased significantly, from 7.1 nm to 20.5 nm. The copper remnants may result from the roughness of the

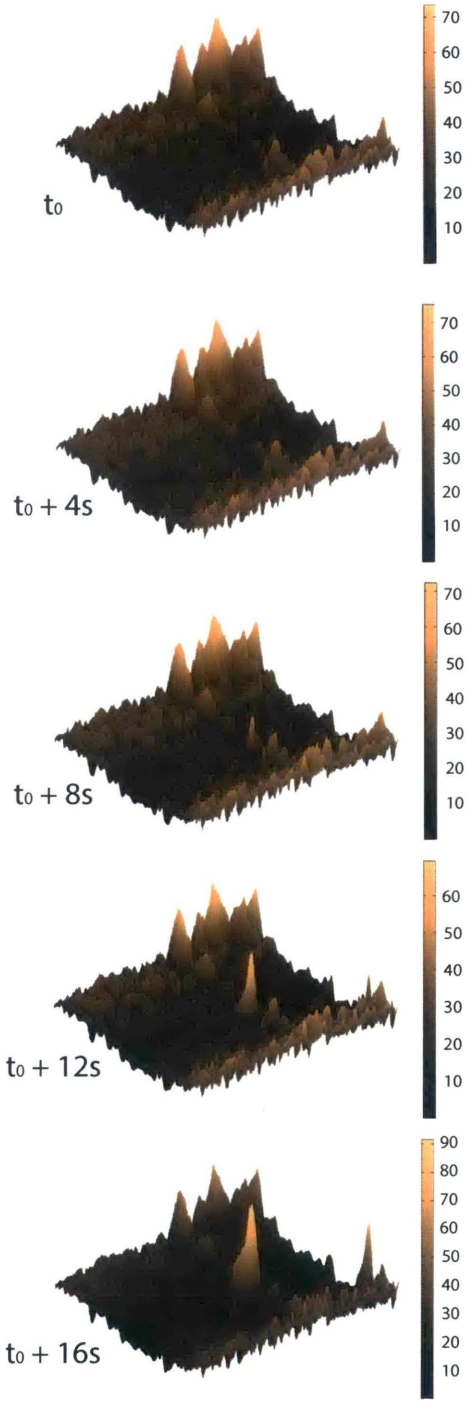

Figure 4-3: Three-dimensional plots showing first stages of nucleation. The nucleate begins in a surface defect at t_0 and will grow to a final height of approximately 300 nm by the end of the voltage sweep. All images show a 3 x 3 μm scan range. Out-of-plane gradient markings are in nanometers.

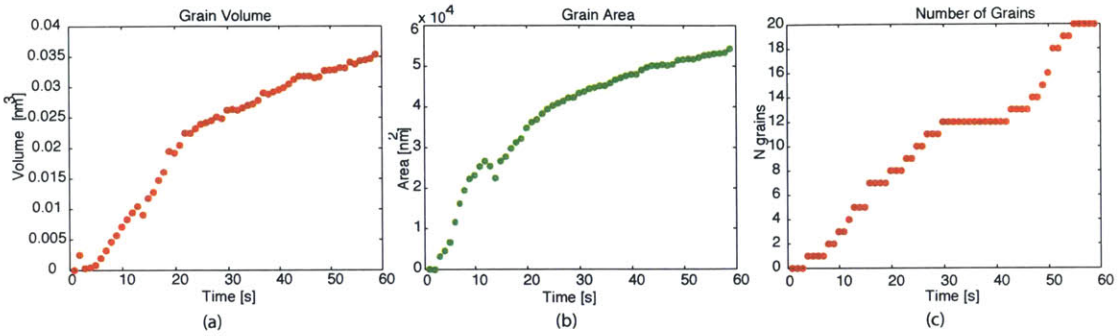

Figure 4-4: Copper grain evolution with time. a) and b) show the evolution of volume and area of the large deposited grain shown in Figs.4-2 and 4-3. c) shows the increase in number of deposited grains with time.

initial sample surface. Additional electrochemical analysis is needed to determine whether these structures are are elemental copper or a gold-copper compound. These residual surface features can be used to study copper deposition and stripping with a different initial surface condition, as is discussed in the following section.

4.3.3 CV on Polycrystalline Substrate with Copper Remnants

After the first CV is performed on the gold substrate, a large positive potential is used to strip remaining copper remnants from the substrate. However, some copper remnants remain on the surface, resulting in an RMS surface roughness of 11.4 nm. This suggests that the remnants may be composed of a gold-copper compound, though additional electrochemical measurements are needed to confirm. In this case, the change in initial surface condition results in completely different deposition behavior. A single mode is seen in which many small grains nucleate on the exposed gold areas, and then coalesce into a copper coating. Nucleation of these grains is shown in Fig. 4-7.

It is also apparent that exposed gold surfaces are strongly favored for deposition. Almost no deposition takes place on the section of the scan area shown in Fig. 4-7 initially covered completely by copper remnants. In addition to the changes in deposition mode, the deposition/stripping cycle effect changes when performed on a surface with initial copper remnants. Figure 4-8 shows the change in the sample

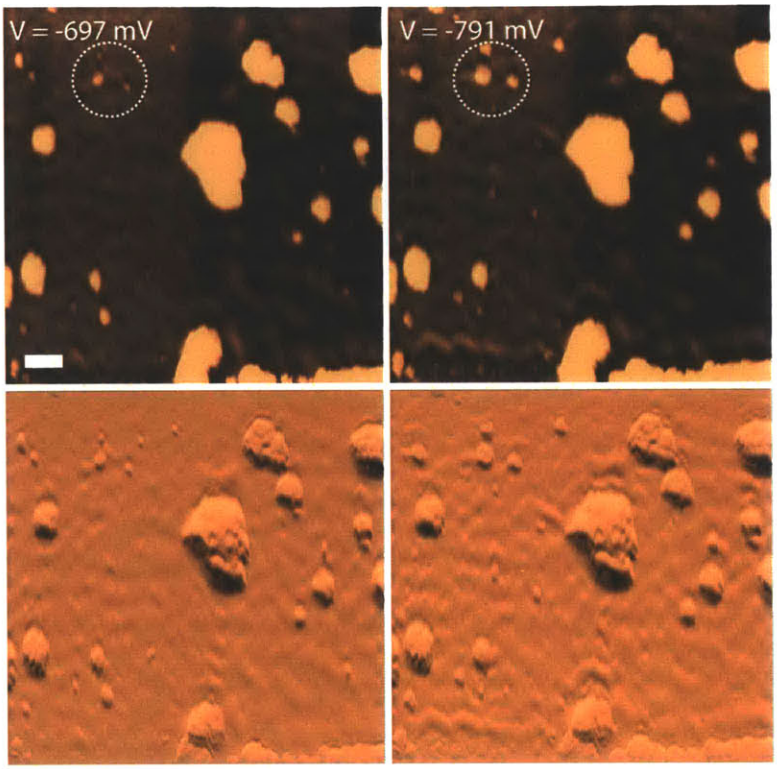

Figure 4-5: Copper deposition on gold from -700 to -800 mV. Small grains develop during this phase, as highlighted by the white dashed circle. Surface corrugations also develop over this period. Between these two effects, the RMS surface roughness increases from 37.8 nm to 45.6 nm between the two frames. Time elapsed between the two frames is 22 seconds. Scale bar is 300 nm. The frames were captured at 256 lines/second, 256 lines/frame, and 1024 samples/line.

surface at the beginning and end of the CV. In this case, the RMS surface roughness remains largely unchanged at approximately 11.4 nm.

4.4 Calcite Dissolution

4.4.1 Experimental Setup

The electrochemical cell described in Chapter 2 is used. Connection ports for electrodes are sealed with wax to prevent leakage. Freshly-cleaved Iceland spar calcite samples (Ward's Scientific) are glued to the sample scanner and immersed in DI water. Acid solution is injected and the dissolution process is observed. In this experiment,

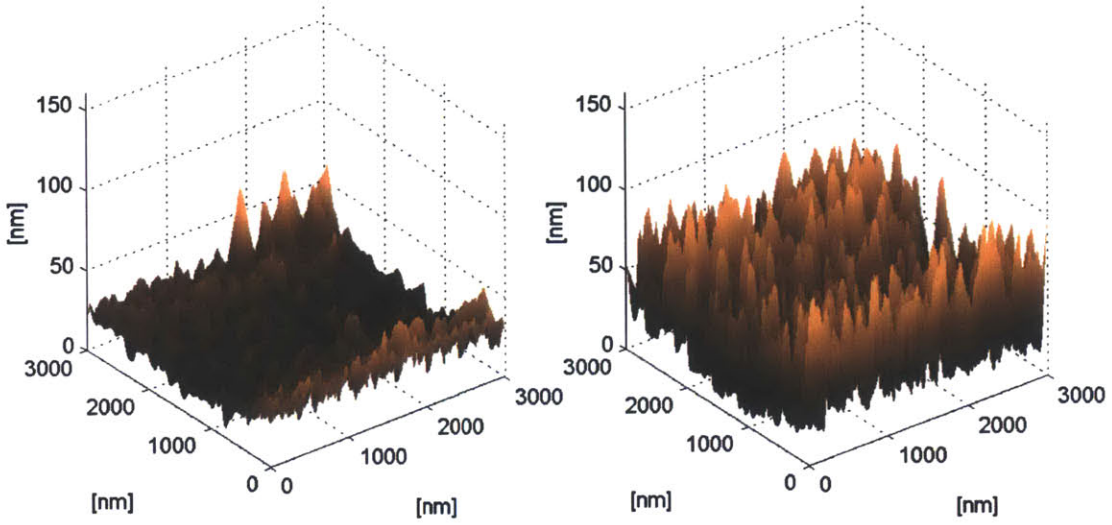

Figure 4-6: Changes in surface roughness between the beginning and end of the cyclic voltammogram trial. Residual copper formations remain on the surface after the stripping phase, resulting in an increase of RMS roughness from 7.1 nm to 20.5 nm. Applied potential is 600 mV in both frames.

dissolution behaviors in two different acid solutions are compared. Hydrochloric (HCl) and sulfuric (H_2SO_4) acid solutions with pH = 1.3 are used. A Bruker FastScan C probe in contact mode was also used in these experiments.

4.4.2 Iceland Spar in Hydrochloric Acid

Dissolution of a freshly cleaved calcite {1014} crystal plane is imaged in hydrochloric acid solution. Figure 4-9 shows an example of the dissolution process.

It is apparent that the dissolution kinetics, while influenced by the calcite crystal structure, are not constrained to single crystal layers. Here, thicker crystal terraces with thicknesses of up to ~30 nm are dissolved away, with the crystal angles matching those expected of the rhombohedral calcite structure. The dissolution is clearly influenced by the orientation of the crystal layers, as shown in Fig. 4-10.

In addition to the dissolution of crystal layers, some grain-like features remain on the edges of the receding layers. The white dashed circles in Fig 4-10 highlight an example of one such feature.

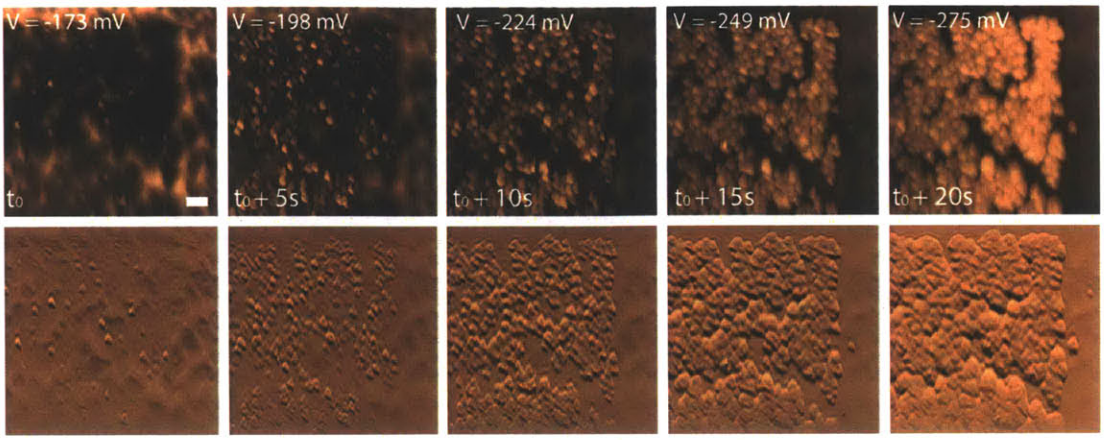

Figure 4-7: Time lapse of copper deposition on gold with initial copper surface features, imaged at 1 frame per second. Nucleates appear on the exposed gold surfaces before coalescing. Deposition is inhibited on the dense initial copper features on in the region on the right side of the frame. Scale bar is 300 nm. Scan speed is 256 lines/second, 1024 samples/line.

4.4.3 Iceland Spar in Sulfuric Acid

Next, dissolution of a freshly cleaved calcite sample in sulfuric acid is observed. Although the pH of the solution is the same as that of the hydrochloric acid trial, the kinetics of dissolution in the sulfuric acid environment show significant differences. First, it is apparent that dissolution begins with pitting at the crystal monolayer level, as shown in Figure 4-11.

After the process develops, dissolution of thick calcite layer begins. Figure 4-12 shows a sequence of this dissolution mode. It is apparent that a very small pit, which shows the expected calcite crystal angles, initiates the dissolution, which develops into dissolution of a thick layer. In this 12-second sequence, the small initial etch pit develops into a dissolving layer 45 nm thick. In general, the sulfuric acid solution seems to be much more aggressive than the hydrochloric solution in calcite dissolution.

4.5 Summary

While high-speed atomic force microscopy has enabled a wealth of discoveries, it has not been applied to materials science and electrochemistry as thoroughly as other

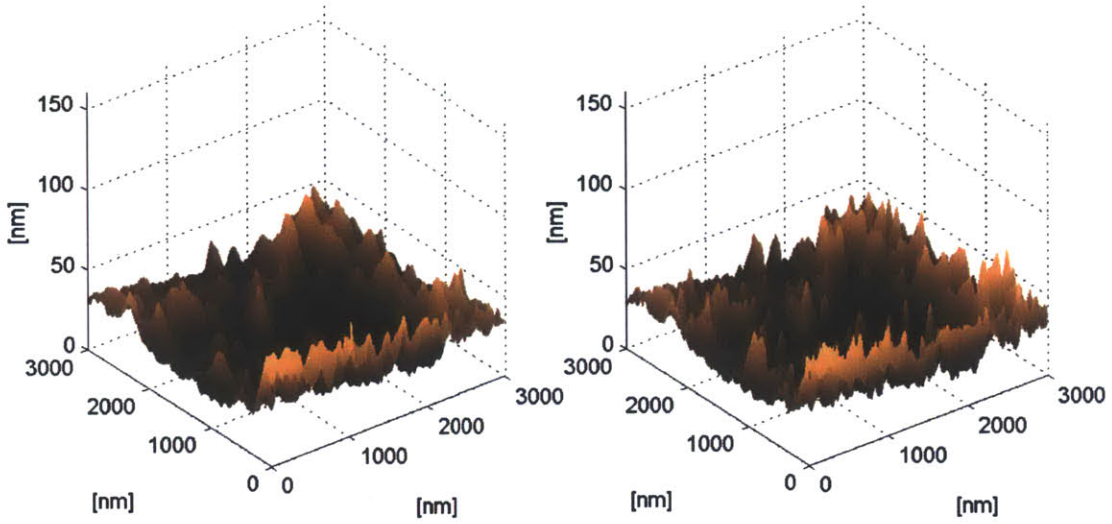

Figure 4-8: Changes in surface roughness between the beginning and end of the cyclic voltammetry trial with initial copper surface features. The sample surface is similar to its initial state after the stripping phase, with no significant change in RMS surface roughness.

fields. Applications in these fields is critical to a wide range of natural and man-made systems. In this work, the modular atomic force microscope presented in earlier chapters is utilized to study two dynamic nanoscale processes.

First, electrochemical deposition of copper on gold is investigated. High-speed AFM images are captured in parallel with electrochemical data to enrich analysis. Cyclic voltammetry (CV) trials are performed. The system is imaged in a custom-made electrochemical cell. The dependence of initial surface condition is clearly shown by the different deposition behaviors during these two CV trials.

Second, calcite dissolution kinetics are observed and compared in hydrochloric and sulfuric acid solutions with low pH. Dissolution in both solutions involves the erosion of thick crystal layers, with thicknesses of ~30 nm in HCl and 45 nm in H_2SO_4. The shape of these layers is influenced by the calcite crystal structure in both cases. In addition, it observed that the sulfuric acid dissolution is initiated by the formation of etch pits at the single layer scale before evolving into removal of thick layers. In general, the sulfuric acid solution is more aggressive. It is evident that, while the H^+ concentrations are equal in the two solutions, the anions play an important role.

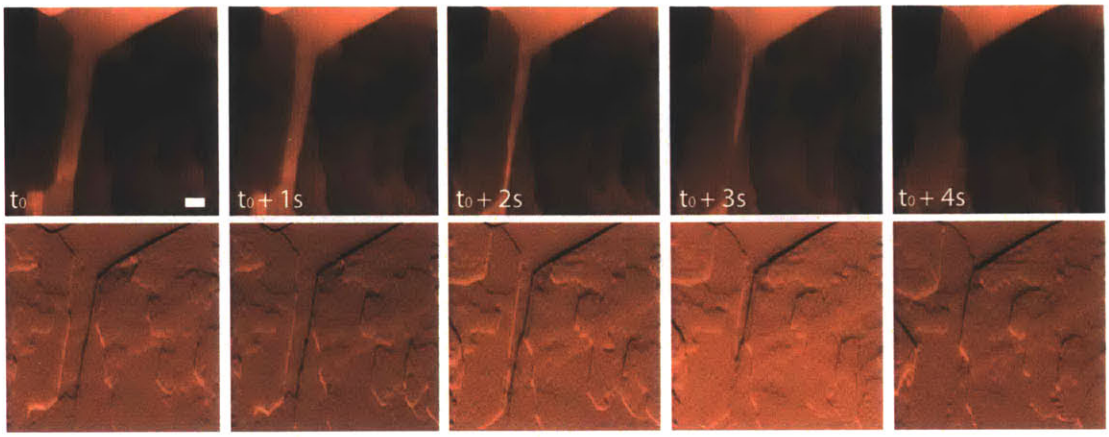

Figure 4-9: Calcite dissolution in pH 1.3 HCl solution. Thick calcite layers are dissolved away. Frames were captured at 1 frame/second. Scan speed is 256 lines/second, 1024 samples/line. Scale bar is 300nm.

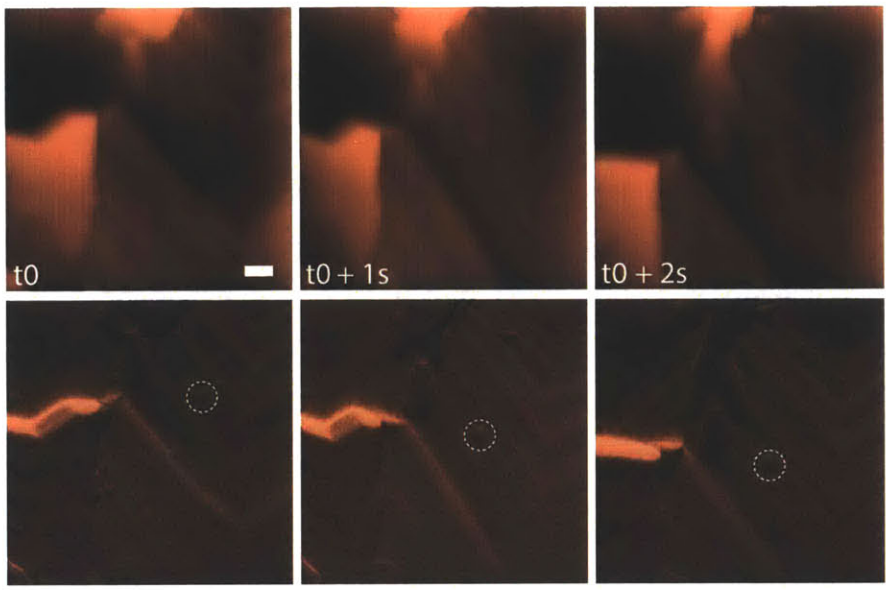

Figure 4-10: Calcite dissolution in pH 1.3 HCl solution, imaged at 1 frame/second. The dissolution of each layer is clearly guided by the crystalline structure. Surface features remain on the edges of the dissolved layers. The white dashed circles highlight one such feature. Scale bar is 300 nm. Scan speed is 256 lines/second, 1024 samples/line.

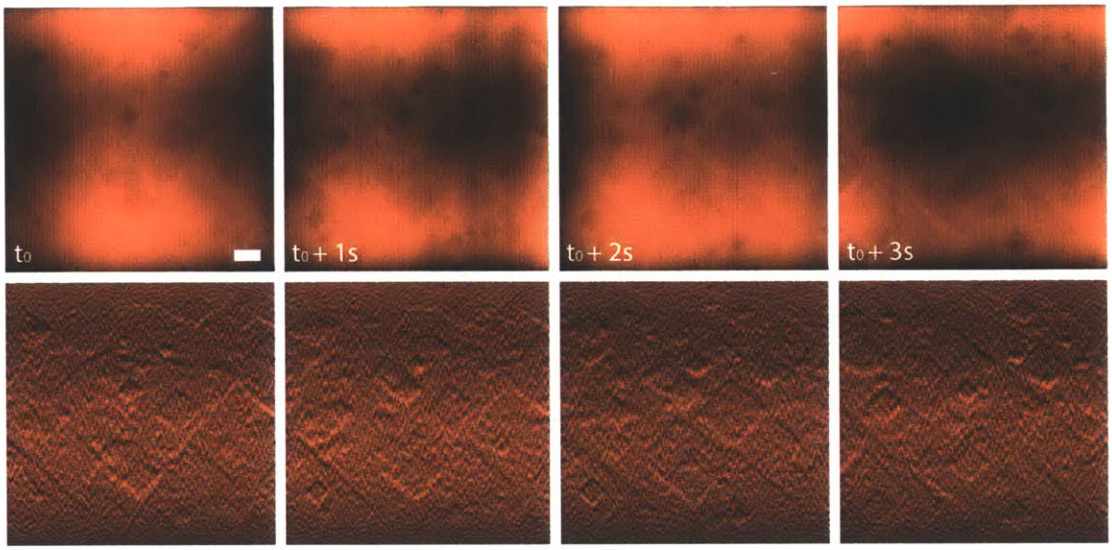

Figure 4-11: Calcite dissolution in pH 1.3 H_2SO_4 solution. At this early stage of dissolution, etch pits of single crystal layers form and coalesce. Nested pits within each etched area eventually lead to erosion of thick layers. Scale bar is 300 nm. Frames were captured at 1 frame/second. Scan speed is 256 lines/second, 1024 samples/line.

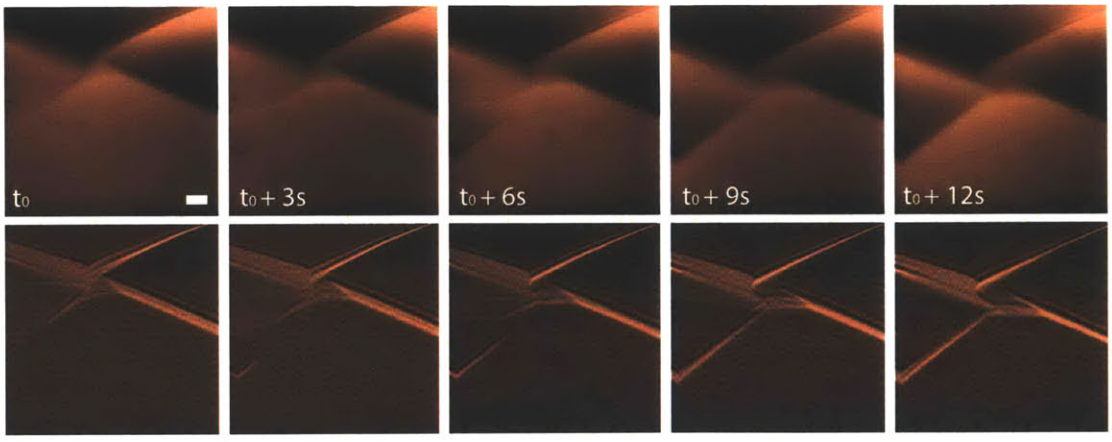

Figure 4-12: Calcite dissolution in H_2SO_4 solution. Frames were captured at 1 frame/second. Initial etch pits evolve into thick dissolving layers. One such feature is shown in this sequence, as it grows from a shallow etch pit along the expected calcite crystalline angles to a deep eroding feature with 45 nm thickness. Scale bar is 500 nm.

Chapter 5

Future Work and Conclusions

5.1 Future Work

The modular atomic force microscope presented in this work will act as a platform for many future studies. The sensing methodology discussed in Chapter 3 will be integrated into the instrument, enabling enhanced capability for in-situ analysis as well as simplification of system identification and controller design and tuning procedures. In addition to the potential for developments in instrument subsystems, the microscope offers the opportunity for many additional imaging studies of dynamic nanoscale processes. Its flexibility to accommodate a variety of sample scanners and cantilever holders for different sample environments will be essential. A brief summary of several such studies are discussed in this section.

5.1.1 Copper Deposition on Gold and Calcite Dissolution

The experiments discussed in Chapter 4 will be continued in order to enrich analysis and gain more insight into these processes. The simultaneous high-speed and large-range performance offered by the multi-actuation methodology is of particular importance in investigations of these samples, as they feature a mix of nanoscale and microscale phenomena.

For future experiments on copper deposition on gold, a flatter gold sample surface,

such as a flame-annealed gold film on mica substrate, can be used to perform the process on a pristine initial sample surface. This type of defect-free surface may allow the complete removal of copper remnants after each CV, allowing for many repeated trials from the same initial surface condition. The integration of out-of-plane sensing, as described in Chapter 3, can be used to improve quantitative measurements of surface changes and grain evolution.

Future work in calcite dissolution could involve additional trials and statistical evaluation and comparison of dissolution kinetics in hydrochloric and sulfuric acids, as well as other solutions. Additional trials may also clarify the role of some of the phenomena observed during these first trials, such as the remnants which remain on the edges of dissolving crystal terraces.

5.1.2 Biofilms

Biofilms are groups of bacteria living on surfaces, usually in aqueous environments. They consist of a matrix of bacteria and extra-cellular substances (typically a mix of sugars, proteins and DNA), which is anchored to the surface. These bacterial formations are ubiquitous in nature, and are responsible for the majority of persistent infections [8]. They are the primary source of hospital-acquired infections, which often result from contaminated tools and implants. Biofilms are highly resistant to disinfectants, though the precise mechanisms of resistance are not clear. In addition to their matrix structure, the bacteria in these colonies exhibit complex signaling behaviors that enhance their resistance.

Video-rate imaging of colonies and individual cells as they react with disinfectants, antibiotics, and other solutions could give insight into the resistive mechanisms of these biofilms. This could lead to enhanced strategies for combating biofilms and the toll they can take on human life. To enable this work, a protocol for growing nonpathogenic biofilms in the lab will need to be developed. A new aqueous sample holder should be built which can accommodate the biofilm growths, as well as appropriate cantilever mounting/actuation for tapping mode imaging.

5.1.3 Self-Assembling Block Copolymers

Self-assembling block copolymers are a class of polymers that self-assemble into patterns when annealed. This method of nanoscale patterning has possible applications in a number of fields, including nanoscale circuitry. They enable small feature sizes (~5 nm) at very low cost. Morphology of the self-assembling block copolymers can be controlled by systematically varying the vapor environment [31]. This assembly has never been visualized in real time.

Study of the self-assembly process with high-speed AFM could yield increased understanding of this nanopatterning method. This work can facilitate development of novel techniques and increased control of the nanofabrication process. To enable the work, a vapor annealing chamber will need to be installed in the AFM. The probe and sample will reside in this chamber, which will also accommodate the annealing solvents (typically hexane and toluene) and gas transfer valves.

5.2 Conclusions

A modular atomic force microscope is presented in order to accelerate the utilization and development of this powerful technology. The modular design of the instrument is discussed, and an AFM is implemented based on the design. The flexibility of the modular AFM is demonstrated by its application to two different imaging tasks which require different configurations. First, copper deposition on gold is imaged with small cantilevers in liquid with a configuration which utilizes coaxial detection, a high-NA objective, and a custom high-speed multi-actuated sample scanner. Second, the mechanical properties of a polymer blend are imaged in tapping mode in air using an off-axis detection configuration with a commercially available piezo tube scanner.

The AFM can be used as a platform for continued research efforts. Here, another need in high-speed AFM is developed towards integration into the instrument. Out-of-plane sensing has not been adequately developed for high-speed imaging applications. This feature enhances the capability for in-situ analysis during high-speed imaging of dynamic nanoscale processes, as well as simplification of system identification and

controller design and tuning. Here, an out-of-plane sensing methodology for dual-actuation out-of-plane positioning is presented. A silicon type strain gauge monitors the low-frequency positioner, while a piezoelectric transducer measures displacement of the high-speed actuator. An annular piezoelectric actuator and inner piezoelectric transducer are used. The effective bandwidth of the nanopositioner is $\sim$70 kHz with compensation, and the total positioning range is 1.93 μm.

Finally, the modular AFM is applied to the study of two dynamic nanoscale processes. Processes in materials science and electrochemistry are essential for many natural and man-made systems, but the application of high-speed AFM in their investigation has not been fully explored. First, electrochemical deposition of copper on gold is investigated. High-speed AFM images are captured in parallel with electrochemical data to enrich analysis. Cyclic voltammetry (CV) trials are performed. The dependence of initial surface condition is clearly shown by the different deposition behaviors during these two CV trials. Second, calcite dissolution kinetics are observed and compared in hydrochloric and sulfuric acid solutions with low pH. Dissolution in both solutions involves the erosion of thick crystal layers, with thicknesses of $\sim$30 nm in HCl and 45 nm in H_2SO_4. The shape of these layers is influenced by the calcite crystal structure in both cases. However, the differences in kinetics between the two solutions indicate that the anions play an important role in the process.

Appendices

Appendix A

Photodiode Circuitry

A.1 Circuit Design

One of the most critical components of the AFM instrumentation is the photodiode detection circuitry. Wide bandwidth and low noise are essential to high-resolution imaging. A four-quadrant photodiode with 25 MHz detection bandwidth is used (Hamamatsu S5980). This photodiode has a large sensing area (25 mm^2 total), which facilitates use with the relatively large beam diameters (small focused spot sizes) needed for small cantilevers.

The photodiode detection circuitry block diagram is shown in Fig. A-1. Currents from each photodiode quadrant are denoted $i_1 \ldots i_4$. The first stage is a series of transimpedance amplifiers which convert these currents to voltages and filter high-frequency noise. Signals from the two quadrants on the top half of the detector are added into v_a, as are those from the bottom half (v_b). The next stage provides additional gain and filtering. A difference amplifier outputs the deflection signal, denoted by Δ. Additionally, a summing amplifier outputs the sum of all the photodiode quadrants, denoted by Σ. This signal is used when adjusting the laser path and focus before imaging. Passive low-pass filters can also be used to remove additional noise from Δ and Σ. In practice, Σ can be filtered aggressively since it is only used for DC adjustment of the incident beam.

We assume that the beam intensity is uniform over a square area with sides equal

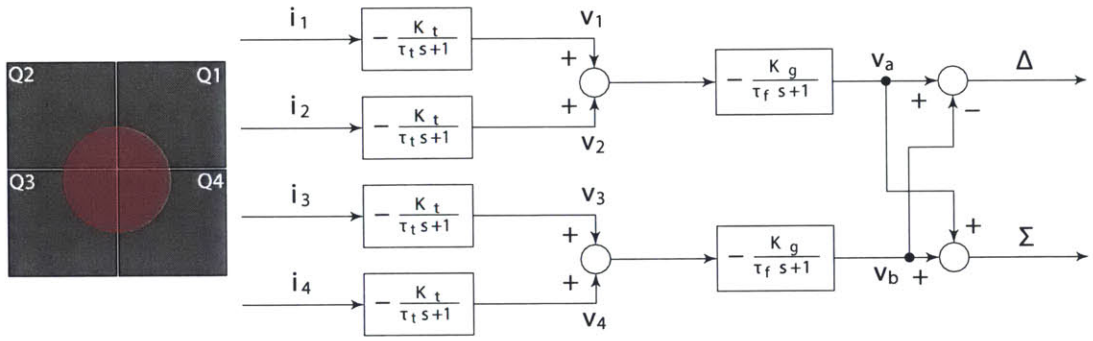

Figure A-1: Photodiode detection circuit block diagram.

to the beam diameter D. This simplifies calculation of system metrics, and gives conservative results since the sensitivity is reduced for a uniform square beam compared to a circular profile of the same total power. The detection sensitivity can be given simply for small probe deflection δ is given by the following

$$\frac{V_o}{\delta} = \frac{2L\alpha KP}{Dl} \tag{A.1}$$

where L is the deflected laser path length, α is the quantum efficiency of the photodiode, K is the total gain of the detection circuitry, P is the total laser power at the photodiode, and l is the length of the cantilever.

The detection noise floor or detection resolution can be calculated with the rearranged equation

$$\delta_{res} = \frac{DlV_{noise}}{2L\alpha KP}. \tag{A.2}$$

A.2 Implementation

Two variants of the circuit are currently used on the instrument, and are shown in Fig. A-2. The circuits differ only in their bandwidth and mechanical mounting features. A wideband circuit with 3 MHz bandwidth is used for high-speed imaging in the coaxial detection configuration. A 700 kHz bandwidth version is used for more conventional imaging conditions in the off-axis detection configuration.

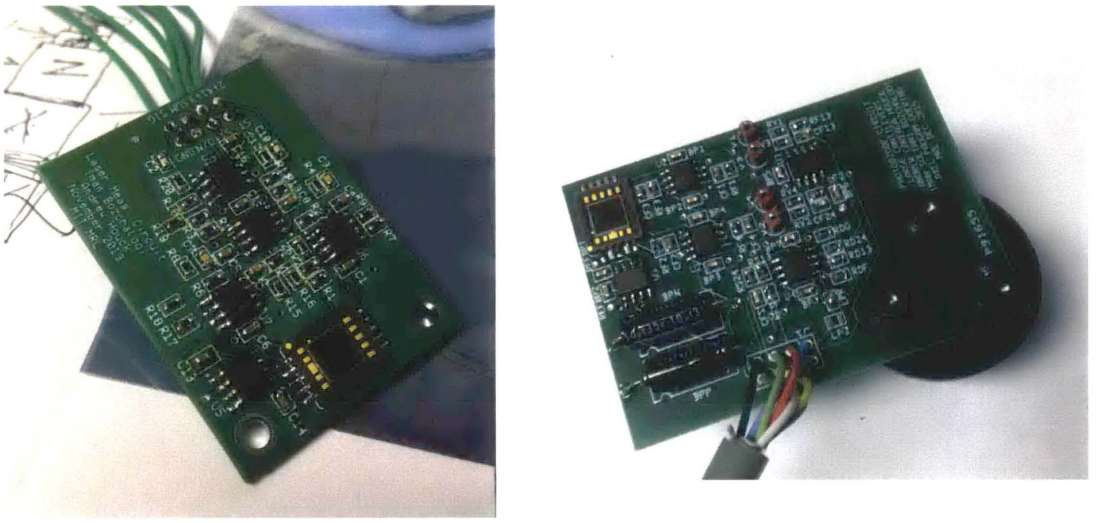

Figure A-2: Photodiode circuits with a) 3 MHz bandwidth for coaxial detection configuration for small cantilevers. b) 700 kHz bandwidth for off-axis detection for large cantilevers.

Appendix B

RF Laser Modulation

B.1 Laser Noise

In its first iteration, the optical head utilized a commercially available laser diode module (Coherent VHK, Edmund 54-021). This type of module has been used in several high-speed AFM research efforts. The wavelength, beam diameter, and output power of the module are 670 nm, 1.1 mm, and 4.9 mW, respectively. In addition to the collimating laser optics, the module contains the laser diode drive circuitry. As a result, a +5 V DC power source is all that is needed to drive the module.

Although the module offers a clean circular beam profile in isolation, the laser exhibited low-frequency drift and erratic instabilities when installed in the instrument, even after a long warm-up time (1-2 hrs.). These behaviors would compromise imaging performance, introducing imaging artifacts or, in the worst case, making the instrument unusable.

This type of laser noise is caused by two primary sources: optical interference noise and optical feedback noise. Optical interference noise arises when reflected or scattered rays reach the photodiode and interfere with other incident rays. This results in low-frequency drifts in the deflection signal. Optical feedback noise is caused by light rays being reflected back up into the amplification cavity of the laser diode. These rays increase mode hop noise. This is more common in the coaxial configuration, since the laser light travels back through the optical system on the way

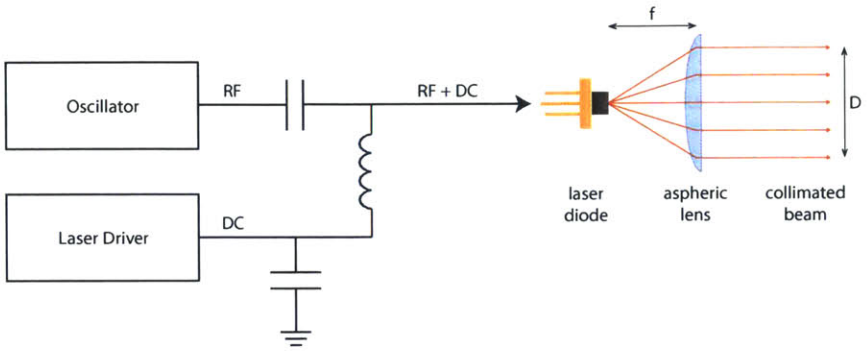

Figure B-1: RF-modulated laser assembly. A high-frequency signal, generated by a voltage-controlled oscillator, is added to the DC current with a bias tee before being injected into a virtual point source laser diode. The light is collimated by a single aspheric lens.

the photodiode. The system is especially susceptible to optical feedback because of the polarizing beamsplitter.

B.2 RF Modulation

These noise sources can be mitigated by RF modulation of the laser, a technique pioneered in hard disk drive research. Optical feedback is common problem in devices such as videodisk optical pickups. In RF modulation, a radio-frequency (RF) signal is superimposed on the DC current normally used to drive the diode. The modulation amplitude, A_m, and DC offset, I_{DC}, are set such that the total injected current dips below the threshold current, I_{th}, during each oscillation. This effectively switches the laser on and off at a high frequency. The modulation frequency, f_{mod}, is typically between 300 and 500 MHz. When the laser diode is initially switched on, it remains in a multimode state for several nanoseconds before settling to a single mode. In this multimode state, it is much less sensitive to modes introduced by reflected rays entering the cavity. By switching the diode on and off at this high frequency, the diode is effectively kept in this multimode state, reducing the effect of optical feedback noise. An added benefit of the method is that it reduces the coherence of the laser, which in turn mitigates the interference noise.

B.3 Implementation

This RF modulation scheme is implemented on the AFM. The VHK module is replaced with a new assembly containing the RF modulation circuitry, laser diode, and collimating optic. A schematic of the setup is shown in Fig. B-1. A benchtop laser diode driver (Newport 505B) generates the DC current, while a voltage controlled oscillator (MiniCircuits POS-400+) generates the RF signal. The oscillation frequency can be set in the range of 200 - 380 MHz via a DC tuning voltage, V_{tune}. The DC and RF signals are added with a bias tee (MiniCircuits PBTC-1GW+) before being injected into the laser diode. A virtual point source laser diode (VPSL-0670-005-X-5-B) is used. Standard laser diodes have asymmetric beam divergence characteristics, which result in an elliptical beam. Using a virtual point source laser diode obviates the need for additional optics to correct for aberrations. This is a 670 nm laser diode with 5 mW maximum power output and 11 degree maximum divergence (off-axis angle is +/- 3 deg). The aspheric collimating lens has a focal length of 6.24 mm, resulting in a nominal beam diameter of 1.95 mm.

Figure B-2: a) RF modulation PCB. The VCO, bias tee, and optical assembly are visible. b) Laser noise reduction to ~50 mV pk-pk for imaging.

B.4 Results

The PCB and laser assembly is shown in Fig. B-2a. Two printed ABS mounting pieces are used to support the assembly after plugging the laser diode into the PCB terminals. After activating the laser diode and adjusting the photodiode circuit, the RF modulation circuitry is switched on to show the effect on noise. Figure B-2 shows the immediate reduction in noise when the RF modulation is turned on. In this case, the noise peak-to-peak amplitude decrease from 800 to 50 mV.

While the RF laser assembly mitigated the noise issues exhibited by the optical head, it is not a complete solution. The overall noise level is not repeatable from experiment to experiment, even when parameters such as oscillation frequency and DC current are kept constant. A more robust solution may be the topic of future research. The added high-frequency content of a square wave, pulsed excitation signal may offer additional improvement.

Appendix C

Breakout Box

C.1 Functionality

A breakout box is constructed for the instrument. The breakout box serves as an access point to various signals, provides signal scaling and filtering, distributes power to various components, and houses additional circuitry. Its primary function is to act as a hub for the various signals and power lines required during instrument operation.

The first group of signals received by the breakout box is the sample scanner actuator signals, which command the y-axis, low-frequency x-axis, high-frequency x-axis, low-frequency out-of-plane, and high-frequency out-of-plane actuators. Each breakout box channel acts as a pre-amplifier, scaling each signal appropriately before its respective high-voltage amplifier. The Z1 and Z2 signals are amplified by a Tech-Project amplifier, while the X1, X2, and Y signals go to custom high-speed amplifier channels. This stage also acts as a first-order low-pass filter, attenuating some high-frequency noise. After being amplified, the high-voltage signals to each actuator are brought back into the breakout box and regrouped, before being sent to the sample scanner with a bundled cable.

The next group of signals into the breakout box is those of the photodiode detection circuitry, for the difference, sum, upper-half sum, and lower-half sum signals. The breakout box simply gives access to these signals. The difference and sum signals are of critical importance for instrument alignment and operation, while the upper-

and lower-half sum signals are available mostly for debugging purposes.

An additional high-speed, high-voltage amplifier channel, as well as the stepper motor driver are housed within the box. The breakout box contains switches for distributing power to the stepper motor, photodiode circuitry, fans, and internal high-speed amplifier channel for small piezoelectric actuators (e.g. tapping mode excitation). Several additional preamplifier channels, as well as power distribution for a DC laser module are included in the current design, though they are not used at present.

C.2 Construction

The breakout box is designed to fit a standard 19-inch rack. The box is shown in Fig. C-1. The front plate is made from aluminum 6061, and the back/sides from acrylic. The two cooling fans mount to the back panel of the box. These are especially useful when using the high-speed amplifier channel mounted in the box, as it utilizes a high-voltage op-amp.

A second iteration of the breakout box could be constructed with a number of improvements. First, features such as additional pre-amplifer channels and DC laser module features could be eliminated to reduce size and complexity. The use of a more modular format, such as Eurocard standard for the different functionalities (photodiode signal access, preamplifier channels, stepper breakout, etc.) would make troubleshooting and upgrading the box more straightforward. Finally, the use of a single AC power line to a wall socket, as well as the required rectification and scaling circuitry, would reduce the need for additional DC power supplies.

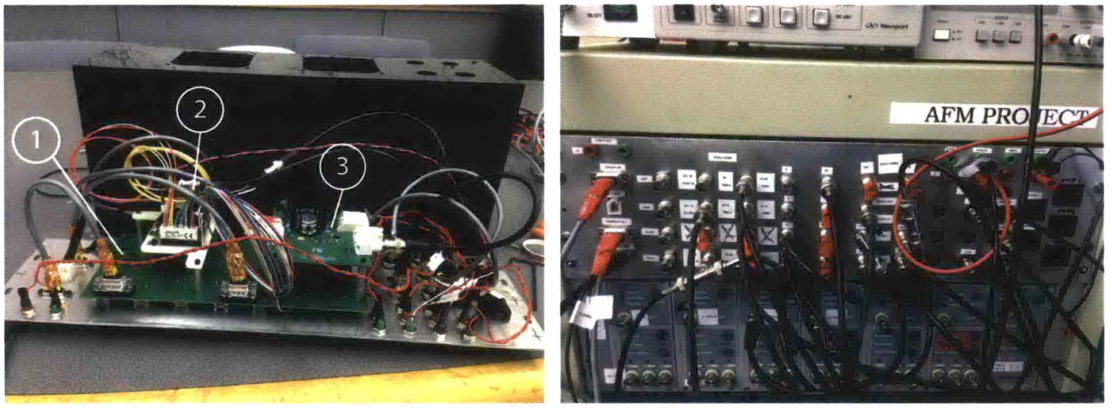

Figure C-1: System breakout box. a) Internal components: 1) Main preamplifier channel board, 2) high-speed amplifier channel, 3) stepper motor driver board. b) Breakout box installed into the instrument rack.

Appendix D

Early Sensing Concepts

D.1 Out-of-plane Sensing with Thin Piezoelectric Transducers

In the early stages of the work, an effort was made to retrofit a sensor to the 1-DOF diaphragm flexure type actuator described in Section 3.5. Instead of replacing the central actuator and fitting an internal sensor, a thin external sensor bonded to the diaphragm surface was used. This method has the benefit that pre-existing nanopositioners could be easily modified with the sensor. Care would need to be taken to prevent and liquid from shorting the contacts of the external sensor. An additional consideration is the fact that the transducer sits between the sample and the actuator. This effect is reduced by the fact that the majority of sensor signal originates from bending of the sensing element, not the axial loads predominately introduced by the sample.

D.2 Results and Discussion

Experiments were performed with two types of thin piezoelectric transducers. Commercially available transducers were used in these initial proof-of-concept tests, but custom-fitted transducers could be developed if needed. Signals from both sensors

were conditioned by a charge mode amplifier, similar to the one presented in Section 3.5. The first was a thin ceramic piezoelectric element, with a thickness of 300 μm (APC International). While this type of element showed high sensitivity and wide bandwidth, the addition of the stiff element disrupted the dynamics of the nanopositioner. To avoid compromising the dynamics of the nanopositioner, the ceramic element was replaced with a polymer film sensor.

A polyvinylidene fluoride (PVDF) piezoelectric film sensor (Measurement Specialties) is used. The transducer is composed of a 28 μm layer of PVDF with silver ink electrodes. Although the sensitivity of the PVDF sensor is not as high as single crystal or ceramic elements, its ability to yield a noninvasive measurement is critical for this application. The sensor is bonded to the diaphragm surface with instant adhesive (Loctite 493).

Figure D-1 shows the normalized dynamic responses of sensor and laser interferometer measurements for Z_2 excitation.

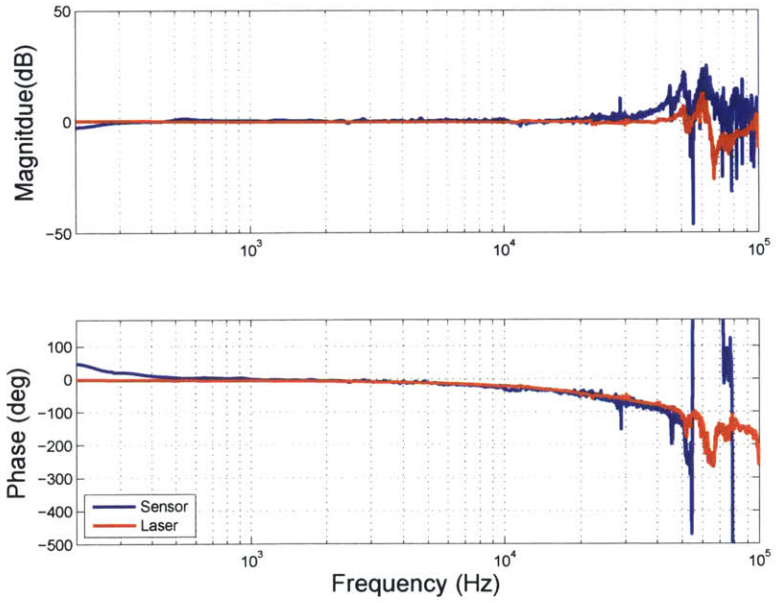

Figure D-1: Frequency response of Z2 nanopositioner. The blue and red curves were measured by a PVDF piezoelectric film sensor and a laser interferometer, respectively.

The sensitivity of the sensor is 3.7 mV/nm in the passband. The high-pass behavior of the piezoelectric transducer is apparent, but does not introduce any phase lead

at frequencies of interest. The low-pass pole also lies sufficiently far from the sensing band to avoid introducing any additional lag. The sensor and laser interferometer measurements are in good agreement, but sensor noise disrupts the reading on the high-frequency end of the sensing band. Noise becomes apparent at $\sim$21 kHz, and continues until the measurements deviate systematically at 30 kHz.

Appendix E

Finite Element Models

The finite element results presented in Chapter 3 were generated using SolidWorks 2014. The diaphragm was modeled as a solid disk of 16 mm diameter and 0.5 mm thickness for static and dynamic simulations. The outer face of the disk was fixed in all simulations. For dynamic simulations, a fixed constraint to the annular actuator cross section (4.5 mm inner diameter, 8 mm outer diameter) was assumed. For static simulation, force was applied uniformly to a 2 x 2 mm face at the diaphragm for the cubic actuator and a 4.5 mm inner diameter, 8 mm outer diameter face for the annular actuator. The simulation material was aluminum 6061 from the standard SolidWorks simulation library. Standard SolidWorks mesh parameters and medium mesh density were used.

Bibliography

[1] D.Y. Abramovitch, S.B. Andersson, Lucy Y. Pao, and Georg Schitter. A tutorial on the mechanisms, dynamics, and control of atomic force microscopes. In *American Control Conference, 2007. ACC '07*, pages 3488–3502, July 2007.

[2] T Ando. High-speed atomic force microscopy coming of age. *NANOTECHNOLOGY*, 23(6), n.d.

[3] T Ando, T Uchihashi, N Kodera, D Yamamoto, M Taniguchi, A Miyagi, and H Yamashita. High-speed atomic force microscopy for observing dynamic biomolecular processes. *JOURNAL OF MOLECULAR RECOGNITION*, 20(6):448 – 458, n.d.

[4] Toshio Ando, Noriyuki Kodera, Eisuke Takai, Daisuke Maruyama, Kiwamu Saito, and Akitoshi Toda. A high-speed atomic force microscope for studying biological macromolecules. *Proceedings of the National Academy of Sciences*, 98(22):12468–12472, 2001.

[5] Toshio Ando, Takayuki Uchihashi, Noriyuki Kodera, Daisuke Yamamoto, Atsushi Miyagi, Masaaki Taniguchi, and Hayato Yamashita. High-speed afm and nano-visualization of biomolecular processes. *Pflügers Archiv - European Journal of Physiology*, 456(1):211–225, 2008.

[6] G. Binnig, C. F. Quate, and Ch. Gerber. Atomic force microscope. *Phys. Rev. Lett.*, 56:930–933, Mar 1986.

[7] G. Binnig and H. Rohrer. Scanning tunneling microscopy. *Surface Science*, 126(13):236 – 244, 1983.

[8] Thomas Bjarnsholt. *Biofilm infections. [electronic resource].* New York ; London : Springer, 2011., 2011.

[9] D Bosbach, L Charlet, B Bickmore, and MF Hochella. The dissolution of hectorite: In-situ, real-time observations using atomic force microscopy. *AMERICAN MINERALOGIST*, 85(9):1209 – 1216, n.d.

[10] I. S. Bozchalooi, K. Youcef-Toumi, D. J. Burns, and G. E. Fantner. Compensator design for improved counterbalancing in high speed atomic force microscopy. *Review of Scientific Instruments*, 82(11):–, 2011.

[11] IS. Bozchalooi and K. Youcef-Toumi. Control design for division and compensation with application to high-speed/large-range nano-positioning. In *American Control Conference (ACC), 2014*, pages 1643–1648, June 2014.

[12] Christoph Braunsmann and Tilman E Schäffer. High-speed atomic force microscopy for large scan sizes using small cantilevers. *Nanotechnology*, 21(22):225705, 2010.

[13] Ignacio Casuso, Felix Rico, and Simon Scheuring. High-speed atomic force microscopy: Structure and dynamics of single proteins. *Current Opinion in Chemical Biology*, 15(5):704 – 709, 2011. Molecular Machines/Analytical Techniques.

[14] Ami Chand, Mario B. Viani, Tilman E. Schaffer, and Paul K. Hansma. Microfabricated small metal cantilevers with silicon tip for atomic force microscopy. *Microelectromechanical Systems, Journal of*, 9(1):112–116, March 2000.

[15] David C. Coffey and David S. Ginger. Patterning phase separation in polymer films with dip-pen nanolithography. *Journal of the American Chemical Society*, 127(13):4564–4565, 2005.

[16] PM Dove and FM Platt. Compatible real-time rates of mineral dissolution by atomic force microscopy (afm). *CHEMICAL GEOLOGY*, 127(4):331 – 338, n.d.

[17] K. El Rifai, O. el Rifai, and K. Youcef-Toumi. On dual actuation in atomic force microscopes. In *American Control Conference, 2004. Proceedings of the 2004*, volume 4, pages 3128–3133 vol.4, June 2004.

[18] N Eliaz and M Eliyahu. Electrochemical processes of nucleation and growth of hydroxyapatite on titanium supported by real-time electrochemical atomic force microscopy. *JOURNAL OF BIOMEDICAL MATERIALS RESEARCH PART A*, 80A(3):621 – 634, n.d.

[19] A.J. Fleming. A review of nanometer resolution position sensors: operation and performance. *Sensors and Actuators A (Physical)*, 190:106 – 126, 2013.

[20] AJ Fleming. Nanopositioning system with force feedback for high-performance tracking and vibration control. *IEEE-ASME TRANSACTIONS ON MECHATRONICS*, 15(3):433 – 447, n.d.

[21] A.J. Fleming, B.J. Kenton, and K.K. Leang. Ultra-fast dual-stage vertical positioning for high performance spms. In *American Control Conference (ACC), 2010*, pages 4975–4980, June 2010.

[22] A.J. Fleming and K.K. Leang. Charge drives for scanning probe microscope positioning stages. *Ultramicroscopy*, 108(12):1551 – 1557, 2008.

[23] A.J. Fleming and K.K. Leang. Charge drives for scanning probe microscope positioning stages. *Ultramicroscopy*, 108(12):1551 – 1557, 2008.

[24] Andrew J. Fleming. Techniques and considerations for driving piezoelectric actuators at high-speed. In *in Proc. SPIE Smart Materials and Structures*, volume 6926, 2008.

[25] Andrew J. Fleming. High-speed vertical positioning for contact-mode atomic force microscopy. In *Advanced Intelligent Mechatronics, 2009. AIM 2009. IEEE/ASME International Conference on*, pages 522–527, July 2009.

[26] Andrew J. Fleming. Dual-stage vertical feedback for high-speed scanning probe microscopy. *Control Systems Technology, IEEE Transactions on*, 19(1):156–165, Jan 2011.

[27] Takeshi Fukuma and Suzanne P. Jarvis. Development of liquid-environment frequency modulation atomic force microscope with low noise deflection sensor for cantilevers of various dimensions. *Review of Scientific Instruments*, 77(4):–, 2006.

[28] Takeshi Fukuma, Masayuki Kimura, Kei Kobayashi, Kazumi Matsushige, and Hirofumi Yamada. Development of low noise cantilever deflection sensor for multienvironment frequency-modulation atomic force microscopy. *Review of Scientific Instruments*, 76(5):–, 2005.

[29] G. Gautschi. *Piezoelectric sensorics : force, strain, pressure, acceleration and acoustic emission sensors, materials and amplifiers / G. Gautschi.* Berlin ; Heidelberg ; New York : Springer, c2002., 2002.

[30] A. Gewirth. Atomic resolution electrochemistry of underpotential deposition processes. In *AIP Conference Proceedings*, number 241, pages 253 – 261, Sch. of Chem. Sci., Illinois Univ., Urbana, IL, USA, 1991.

[31] KW Gotrik, AF Hannon, JG Son, B Keller, A Alexander-Katz, and CA Ross. Morphology control in block copolymer films using mixed solvent vapors. *ACS NANO*, 6(9):8052 – 8059, 2013.

[32] W.T. Higgins. A comparison of complementary and kalman filtering. *Aerospace and Electronic Systems, IEEE Transactions on*, AES-11(3):321–325, May 1975.

[33] P.E. Hillner, S. Manne, P.K. Hansma, and A.J. Gratz. Atomic-scale imaging of calcite growth and dissolution in real time. *Geology; (United States)*, page 359, 1992.

[34] S. Hosaka, K. Etoh, A. Kikukawa, and H. Koyanagi. Megahertz silicon atomic force microscopy (afm) cantilever and high-speed readout in afm-based recording. *Journal of Vacuum Science and Technology B*, 18(1):94–99, 2000.

[35] Michael E. Hyde, Robert Jacobs, and Richard G. Compton. In situ afm studies of metal deposition. *The Journal of Physical Chemistry B*, 106(43):11075–11080, 2002.

[36] Younkoo Jeong, G. R. Jayanth, and Chia-Hsiang Menq. Control of tip-to-sample distance in atomic force microscopy: A dual-actuator tip-motion control scheme. *Review of Scientific Instruments*, 78(9):–, 2007.

[37] Omid Karoussi, Lone L. Skovbjerg, Tue Hassenkam, S.L. Svane Stipp, and Aly A. Hamouda. Afm study of calcite surface exposed to stearic and heptanoic acids. *Colloids and Surfaces A: Physicochemical and Engineering Aspects*, 325:107 – 114, 2008.

[38] Brian J. Kenton, Andrew J. Fleming, and Kam K. Leang. Compact ultra-fast vertical nanopositioner for improving scanning probe microscope scan speed. *Review of Scientific Instruments*, 82(12):–, 2011.

[39] Noriyuki Kodera, Daisuke Yamamoto, Ryoki Ishikawa, and Toshio Ando. Video imaging of walking myosin v by high-speed atomic force microscopy. *Nature*, 468(7320), 2010.

[40] Noriyuki Kodera, Hayato Yamashita, and Toshio Ando. Active damping of the scanner for high-speed atomic force microscopy. *Review of Scientific Instruments*, 76(5):–, 2005.

[41] S. Kuiper and G. Schitter. Active damping of a piezoelectric tube scanner using self-sensing piezo actuation. *Mechatronics*, 20(6):656 – 665, 2010.

[42] Schitter G. Kuiper S, Fleming AJ. Dual actuation for high speed atomic force microscopy. In *5th IFAC Symposium on Mechatronic Systems*, page 220, 2010.

[43] Mo Li, H. X. Tang, and M. L. Roukes. Ultra-sensitive nems-based cantilevers for sensing, scanned probe and very high-frequency applications. *Nature Nanotechnology*, 2:114–120, 2007.

[44] Y.G. LI and A. LASIA. Study of gold deposition on copper by electrochemical and microscopic techniques. *Journal of Applied Electrochemistry*, 27(6):643–650, 1997.

[45] I A Mahmood and S O Reza Moheimani. Fast spiral-scan atomic force microscopy. *Nanotechnology*, 20(36):365503, 2009.

[46] I.a. Mahmood and S. Moheimani. Tracking Control of a Nanopositioner Using Complementary Sensors. *IEEE Transactions on Nanotechnology*, 8(1):55–65, January 2009.

[47] H. J. Mamin, H. Birk, P. Wimmer, and D. Rugar. High-speed scanning tunneling microscopy: Principles and applications. *Journal of Applied Physics*, 75(1), 1994.

[48] S. Manne, P. K. Hansma, J. Massie, V. B. Elings, and A. A. Gewirth. Atomic-resolution electrochemistry with the atomic force microscope: Copper deposition on gold. *Science*, (4990):183, 1991.

[49] S O Reza Moheimani and Yuen K Yong. Simultaneous sensing and actuation with a piezoelectric tube scanner. *The Review of scientific instruments*, 79(7):073702, July 2008.

[50] B. Mokaberi and Aristides A.G. Requicha. Compensation of scanner creep and hysteresis for afm nanomanipulation. *Automation Science and Engineering, IEEE Transactions on*, 5(2):197–206, April 2008.

[51] C.V. Newcomb and I. Flinn. Improving the linearity of piezoelectric ceramic actuators. *Electronics Letters*, 18(11):442 – 444, 1982.

[52] HadiăTavakoli Nia, ImanăS. Bozchalooi, Yang Li, Lin Han, Han-Hwa Hung, Eliot Frank, Kamal Youcef-Toumi, Christine Ortiz, and Alan Grodzinsky. High-bandwidth afm-based rheology reveals that cartilage is most sensitive to high loading rates at early stages of impairment. *Biophysical Journal*, 104(7):1529 – 1537, 2013.

[53] R. Pearce and G.J. Vancso. Real-time imaging of melting and crystallization in poly(ethylene oxide) by atomic force microscopy. *Polymer*, 39(5):1237 – 1242, 1998.

[54] Alice Pyne, Will Marks, Loren M Picco, Peter G Dunton, Arturas Ulcinas, Michele E Barbour, Siân B Jones, James Gimzewski, and Mervyn J Miles. High-speed atomic force microscopy of dental enamel dissolution in citric acid. *Archives Of Histology And Cytology*, 72(4-5):209 – 215, 2009.

[55] HJ Qi, K Joyce, and MC Boyce. Durometer hardness and the stress-strain behavior of elastomeric materials. *RUBBER CHEMISTRY AND TECHNOLOGY*, 76(2):419 – 435, 2003.

[56] E. Ruiz-Agudo, C.V. Putnis, C. Jiménez-López, and C. Rodriguez-Navarro. An atomic force microscopy study of calcite dissolution in saline solutions: The role of magnesium ions. *Geochimica et Cosmochimica Acta*, 73(11):3201 – 3217, 2009.

[57] G Schitter, F Allgöwer, and A Stemmer. A new control strategy for high-speed atomic force microscopy. *Nanotechnology*, 15(1):108, 2004.

[58] G. Schitter, P. Menold, H. F. Knapp, F. Allgöwer, and A. Stemmer. High performance feedback for fast scanning atomic force microscopes. *Review of Scientific Instruments*, 72(8), 2001.

[59] Georg Schitter, K.J. Astrom, Barry E. DeMartini, P.J. Thurner, K.L. Turner, and Paul K. Hansma. Design and modeling of a high-speed afm-scanner. *Control Systems Technology, IEEE Transactions on*, 15(5):906–915, Sept 2007.

[60] Georg Schitter, W.F. Rijkee, and N. Phan. Dual actuation for high-bandwidth nanopositioning. In *Decision and Control, 2008. CDC 2008. 47th IEEE Conference on*, pages 5176–5181, Dec 2008.

[61] A. Sebastian, M.V. Salapaka, and Jason P. Cleveland. Robust control approach to atomic force microscopy. In *Decision and Control, 2003. Proceedings. 42nd IEEE Conference on*, volume 4, pages 3443–3444 vol.4, Dec 2003.

[62] R Shiraki, PA Rock, and WH Casey. Dissolution kinetics of calcite in 0.1 m nacl solution at room temperature: An atomic force microscopic (afm) study. *AQUATIC GEOCHEMISTRY*, 6(1):87 – 108, 2000.

[63] I. Soltani Bozchalooi and Youcef-Toumi K. Multi-actuation and pi control: A simple recipe for high-speed and large-range atomic force microscopy. *Ultramicroscopy*, 146:117–124, 2014.

[64] T. Sulchek, S. C. Minne, J. D. Adams, D. A. Fletcher, A. Atalar, C. F. Quate, and D. M. Adderton. Dual integrated actuators for extended range high speed atomic force microscopy. *Applied Physics Letters*, 75(11), 1999.

[65] Yuki Suzuki, Nobuaki Sakai, Aiko Yoshida, Yoshitsugu Uekusa, Akira Yagi, Yuka Imaoka, Shuichi Ito, Koichi Karaki, and Kunio Takeyasu. High-speed atomic force microscopy combined with inverted optical microscopy for studying cellular events. *Scientific Reports*, 3, 2013.

[66] Joel Therrien, Amir Dindar, and David Smith. Afm studies of nanoparticle deposition via electrospray ionization. *Microscopy Research and Technique*, 70(6):530–533, 2007.

[67] T Uchihashi, R Iino, T Ando, and H Noji. High-speed atomic force microscopy reveals rotary catalysis of rotorless f-1-atpase. *SCIENCE*, 333(6043):755 – 758, n.d.

[68] Takayuki Uchihashi, Noriyuki Kodera, and Toshio Ando. Guide to video recording of structure dynamics and dynamic processes of proteins by high-speed atomic force microscopy. *Nature Protocols*, 7:11931206, 2012.

[69] M. B. Viani, T. E. Schäffer, G. T. Paloczi, L. I. Pietrasanta, B. L. Smith, J. B. Thompson, M. Richter, M. Rief, H. E. Gaub, K. W. Plaxco, A. N. Cleland, H. G. Hansma, and P. K. Hansma. Fast imaging and fast force spectroscopy of single biopolymers with a new atomic force microscope designed for small cantilevers. *Review of Scientific Instruments*, 70(11), 1999.

[70] Mario B. Viani, Tilman E. Schäffer, Ami Chand, Matthias Rief, Hermann E. Gaub, and Paul K. Hansma. Small cantilevers for force spectroscopy of single molecules. *Journal of Applied Physics*, 86(4), 1999.

[71] Sachin P. Wadikhaye, Yuen Kuan Yong, and S. O. Reza Moheimani. A serial-kinematic nanopositioner for high-speed atomic force microscopy. *Review of Scientific Instruments*, 85(10):–, 2014.

[72] D. A. Walters, J. P. Cleveland, N. H. Thomson, P. K. Hansma, M. A. Wendman, G. Gurley, and V. Elings. Short cantilevers for atomic force microscopy. *Review of Scientific Instruments*, 67(10), 1996.

[73] M.J. Williamson, R.M. Tromp, P.M. Vereecken, R. Hull, and F.M. Ross. Dynamic microscopy of nanoscale cluster growth at the solid-liquid interface. *Nature Materials*, 2(8):532 – 536, 2003.

[74] Yan Yan, Ying Wu, Qingze Zou, and Chanmin Su. An integrated approach to piezoactuator positioning in high-speed atomic force microscope imaging. *Review of Scientific Instruments*, 79(7):–, 2008.

[75] Y. K. Yong, S. O. R. Moheimani, B. J. Kenton, and K. K. Leang. Invited review article: High-speed flexure-guided nanopositioning: Mechanical design and control issues. *Review of Scientific Instruments*, 83(12):–, 2012.

[76] Y.K. Yong and S.O.R. Mohemani. Design of an inertially counterbalanced z -nanopositioner for high-speed atomic force microscopy. *Nanotechnology, IEEE Transactions on*, 12(2):137–145, March 2013.

[77] Yuen Kuan Yong, Andrew J. Fleming, and S. O. Moheimani. A Novel Piezoelectric Strain Sensor for Simultaneous Damping and Tracking Control of a High-Speed Nanopositioner. *IEEE/ASME Transactions on Mechatronics*, 18(3):1113–1121, June 2013.

[78] Haimei Zheng, Rachel K. Smith, Young-wook Jun, Christian Kisielowski, Ulrich Dahmen, and A. Paul Alivisatos. Observation of single colloidal platinum nanocrystal growth trajectories. *Science*, (5932):1309, 2009.